

Dissertation

Sub-Femtosecond XUV Pulse Generation and Measurement

ausgeführt zum Zwecke der Erlangung des akademischen Grades eines
Doktors der technischen Wissenschaften
unter der Leitung von

Univ.-Prof. Dr. Ferenc Krausz
Institut für Photonik, E 387

eingereicht an der Technischen Universität Wien
Fakultät für Elektrotechnik und Informationstechnik

von

Dipl.-Ing. Reinhard Kienberger
9026531
1080 Wien, Albertplatz 8/10

Wien, im Juni 2002

Danksagung

Mein besonderer Dank gilt meinem Zimmerkollegen Dr. Michael Hentschel, der einen Großteil der Versuche gemeinsam mit mir durchgeführt und viele Nächte - meistens im Labor - mit mir verbracht hat. Vielen Dank richte ich an meine Kollegen Dipl.-Ing. Matthias Uiberacker, Marco Hornung, Univ.-Doz. Dr. Matthias Lenzner, Priv.-Doz. Dr. Markus Drescher und a.o. Univ.-Prof. Dr. Georg Reider, die mir mit Rat und Tat und auch als kameradschaftliche Kollegen zur Seite standen.

Meinem "Lehrmeister", Univ.-Doz. Dr. Matthias Schnärer, danke ich für die Weitergabe seiner reichhaltigen Erfahrungen im Laborbetrieb. Eine Fundgrube verschüttet geglaubter Informationen war mir a.o. Univ.-Prof. Dr. Christian Spielmann, hierfür sei herzlich gedankt. Dem Alt-Institutsvorstand O. Univ.-Prof. Dr. Arnold Schmidt sowie den weiteren Kollegen am Institut für Photonik sei für das hervorragende kollegiale Arbeitsklima gedankt.

Den Sekretärinnen Dietlinde Egger, Blanka Dvorsak, Eva Sturm und Elfriede Lohwasser sowie Herrn Ing. Anton Brückl danke ich vielmals für die Unterstützung in administrativen bzw. technischen Belangen.

Besonderer Dank gilt meinem Doktorvater, Univ.-Prof. Dr. Ferenc Krausz, der mit seinem ungebremsten Elan immer auf den Fortgang der Versuche bedacht war und mich mit der Umsetzung seiner zahllosen Ideen auf Trab hielt.

Für die große Unterstützung auch im Doktoratsstudium danke ich sehr herzlich meinen Eltern.

Nicht zuletzt danke ich auf das herzlichste meiner künftigen Frau Katharina für die Geduld, die sie in den letzten Wochen mir gegenüber bewiesen hat.

Kurzfassung

Der Einblick in immer kleinere mikroskopische Einheiten der Materie sowie in immer kürzere Abläufe chemischer, physikalischer oder atomarer Prozesse bringt wichtige Aufschlüsse für die technische Grundlagenforschung. Dies ist eine Triebfeder für die Entwicklung von Techniken, die einen solchen Einblick ermöglichen.

Die Auflösung einer zeitaufgelösten Messung ist durch die "Belichtungszeit" begrenzt, eine Tatsache, die aus der Photographie allgemein bekannt ist, aber vor allem bei Messungen auf einer Ultrakurzzeit-Skala eine große Herausforderung darstellt. Etliche Prozesse im atomaren oder gar subatomaren Bereich finden auf einer sub-femtosekunden Zeitskala ($1 \text{ fs} = 10^{-15} \text{ s}$) statt. Um sie zeitaufgelöst - etwa mit sogenannten "pump-probe" Versuchen - darstellen zu können, benötigt man elektromagnetische Pulse, deren Dauer unter einer Femtosekunde liegt. Der Dauer solcher Pulse im sichtbaren Bereich, wie sie durch Laserlicht erzeugt werden können, ist jedoch durch die Natur eine Grenze gesetzt. Da ein einziger Oszillationszyklus zum Beispiel bei einer Wellenlänge von 780 nm eine Dauer von ca. 2,6 fs aufweist, stellt dies in der Praxis eine Untergrenze der Pulsdauer dar. Schon vor dem Jahr 2000 war man soweit, mit Ultrakurzpuls-Lasertechnik Pulsdauern unter zwei Oszillationsperioden zu erzeugen. Um kürzere Pulsdauern zu erreichen, müsste man sich also in Richtung kürzerer Wellenlängen in den XUV- (Extrem Ultraviolett) bzw. Röntgenbereich bewegen. Im Kapitel 1, "Motivation", wird diese Problematik, einige Prozesse im Sub-Femtosekunden-Bereich sowie die Notwendigkeit kurzer Wellenlängen besprochen.

Eine äußerst gute Methode einer derartigen Frequenzkonversion, bei der die zeitliche und räumliche Kohärenz der treibenden Laserstrahlung erhalten bleibt, ist die sogenannte "High-Order Harmonic Generation (HHG)". Sie ist das in dieser Arbeit verwendete Grundprinzip der Generierung von Sub-Femtosekunden-Pulsen und wird in Kapitel 2, "Generation of sub-femtosecond pulses", besprochen. Dazu wird zunächst

das verwendete Lasersystem vorgestellt, das Prinzip der High-Order Harmonic Generation erläutert sowie anhand von Versuchsergebnissen die Möglichkeit der Erzeugung von Sub-Femtosekunden-Pulsen besprochen.

Kapitel 3, "Measurement of sub-femtosecond pulses", widmet sich der Messung von Sub-Femtosekunden-Pulsen, was mit "herkömmlichen" Methoden nicht möglich ist. Die Probleme, die etwa bei der Messung über eine Autokorrelation entstehen, werden ebenso erörtert wie das in dieser Arbeit verwendete Prinzip der Kreuzkorrelation zwischen den XUV Pulsen und sichtbarem Laserlicht. Der zugrundeliegende nichtlineare Prozess der Photoionisation, die Messung von Photoelektronenspektren, spektrale Vorgänge bei zeitlicher Überlappung von XUV- und fundamentalem Laserpuls sowie die auf den Messergebnissen basierende Berechnung der Pulsdauer werden dargestellt.

Im Kapitel 4, "Time-resolved attosecond spectroscopy", werden bereits durchgeführte und geplante Experimente zur Anwendung der erzeugten Sub-Femtosekunden-Pulse, speziell im Bereich der Spektroskopie, vorgestellt.

Eine Diskussion über die Bedeutung, Verwendbarkeit der Ergebnisse dieser Arbeit sowie technische Verbesserungsmöglichkeiten bilden in Kapitel 5, "Conclusion" den Abschluss.

Eine Liste der Publikationen und Konferenzbeiträge, die auf der für diese Dissertation getätigten Arbeit basieren, findet sich im Anhang an die Zusammenfassung in englischer Sprache, im nächsten Kapitel, "Summary".

Summary

Abstract

The generation of ever shorter pulses is a key to exploring the dynamic behaviour of matter on ever shorter time scales. Recent developments have pushed the duration of laser pulses close to its natural limit, to the wave cycle, which lasts somewhat longer than one femtosecond ($1 \text{ fs} = 10^{15} \text{ s}$) in the visible spectral range. Time-resolved measurements with these pulses are able to trace dynamics of molecular structure but fail to capture electronic processes occurring in atoms on an attosecond ($1 \text{ as} = 10^{18} \text{ s}$) time scale. The generation of high-order harmonic radiation in the extreme ultraviolet and soft x-ray regime from atoms exposed to intense few-femtosecond-duration laser pulses comprising just a few wave cycles opened the way to the generation of isolated XUV/x-ray pulses shorter than 1 femtosecond. This 'Dissertation' will focus on the generation and measurement of these pulses (metrology) and discuss possible ways of using these atomic-time-scale bursts of electromagnetic radiation for tracking ultrafast electronic processes with attosecond resolution (spectroscopy).

Summary

The insight in always smaller microscopic units of matter as well as in always shorter courses of chemical, physical or atomic processes give important information used for basic research. This is a driving force for the development of techniques allowing such informative insight.

The resolution of time resolved measurements is limited by the exposure time, a fact, which is well known from photography, and constitutes a formidable challenge on ultrashort timescales. A wide range of processes in the atomic or sub-atomic regime

take place on a sub-femtosecond timescale ($1 \text{ fs} = 10^{-15} \text{ s}$). To make snapshots of these events - e.g. with so called 'pump-probe' experiments, electromagnetic pulses having a duration below one femtosecond are required. Nature, however, sets a limit to such pulses in the visible range, as they can be produced by laser light. At a wavelength of 780 nm, for instance, one oscillation cycle lasts for 2.6 fs, setting a practical lower limit of the pulse-duration. By the end of the past millenium pulse durations were shortened below two oscillation cycles using ultrashort-laser techniques. In order to reach even shorter pulse durations, one has to move towards shorter wavelengths in the XUV (extreme ultraviolet) respectively x-ray regime. Chapter 1, 'Motivation' points out these problems, several processes in the sub-femtosecond regime and the necessity of shorter wavelengths.

A reliable and well known method of such a frequency conversion, providing the preservation of temporal and spatial coherence like from the driving laser radiation, is what has been referred to as 'High-Order Harmonic Generation (HHG)'. It is the main principle of generating sub-femtosecond pulses used in this work and will be discussed in Chapter 2, 'Generation of sub-femtosecond pulses'. Here, the applied laser system will be presented, the principle of High-Order Harmonic Generation will be explained, and the possibility of generating sub-femtosecond pulses will be discussed based on experimental results.

Chapter 3, 'Measurement of sub-femtosecond pulses', addresses the measurement on this timescale, which is not feasible by conventional methods. Problems frustrating extension of the auto-correlation method into the deep XUV/soft x-ray regime will be explained as well as the principle of cross-correlation between XUV-pulses and visible light, which was applied in this work. The non-linear process of photo-ionization, measurement of photo-electron spectra, electronic dynamics occurring at the temporal overlap between XUV- and fundamental laser pulses and the evaluation of the pulse duration from the experimental results will be elaborated.

In Chapter 4, 'Time-resolved attosecond spectroscopy', experiments that have already been carried out or are being planned, especially in the field of spectroscopy using sub-femtosecond XUV-pulses, will be presented.

A discussion of the significance and implications of the results and possible technical improvements is presented in Chapter 5, 'Conclusion'.

The work carried out with several coworkers resulted the following publications:

- ² R. Kienberger, M. Hentschel, M. Uiberacker, Ch. Spielmann, M. Kitzler, A. Scrinzi, M. Wieland, Th. Westerwalbesloh, U. Kleineberg, U. Heinzmann, M. Drescher, F. Krausz: Steering attosecond electron wavepackets with light, **Science** (2002), accepted, to be published.
- ² R. Kienberger, M. Hentschel, C. Spielmann, G. Reider, N. Milosevic, M. Drescher, U. Heinzmann, F. Krausz: Sub-femtosecond x-ray pulse generation and measurement, **Applied Physics B** **74** (2002), 1-7 , **(invited)**.
- ² M. Hentschel, R. Kienberger, C. Spielmann, G. Reider, N. Milosevic, T. Brabec, P. Corkum, U. Heinzmann, M. Drescher, F. Krausz: Attosecond metrology, **Nature** **414** (2001), 509 - 513.
- ² M. Drescher, M. Hentschel, R. Kienberger, G. Tempea, Ch. Spielmann, G. Reider, P.B. Corkum, F. Krausz, X-Ray Pulses Approaching the Attosecond Frontier, **Science** **291** (2001), 1923.
- ² M. Schöffner, Ch. Streli, P. Wobrauschek, M. Hentschel, R. Kienberger, Ch. Spielmann, F. Krausz, Femtosecond X-Ray Fluorescence, **Phys. Rev. Lett.** **85** (2000), 3392 .

The results of the thesis have been or will be presented by me or colleagues at several international conferences:

- ² R. Kienberger, M. Hentschel, M. Drescher, G.A. Reider, C. Spielmann, F. Krausz: Sub-fs X-ray pulse generation and measurement; 2002 Conference on Lasers and Electro-Optics, Long Beach, California, USA **(invited)**; 19.05.2002 - 24.05.2002;
- ² R. Kienberger, M. Hentschel, C. Spielmann, G.A. Reider, M. Drescher, F. Krausz: Sub-fs X-ray pulse generation and measurement; Seminar on Fundamentals of Laser Interactions III, K  htai, Tirol, Austria **(invited)**; 13.01.2002 - 18.01.2002; in: Book of Abstracts; (2002), S. 15.
- ² R. Kienberger, M. Hentschel, M. Drescher, G.A. Reider, C. Spielmann, F. Krausz: Breaking the 1-femtosecond barrier: the advent of attosecond metrology;

- 2002 Nonlinear Optics Conference OSA, Wailea, Maui, Hawaii, USA (**invited**); 29.07.2002 - 02.08.2002;
- ² R. Kienberger, M. Hentschel, M. Drescher, G.A. Reider, C. Spielmann, F. Krausz: Sub-fs X-ray pulse generation and measurement; 2002 OSA annual meeting, Orlando, Florida, USA (**invited**); 29.09.2002 - 03.10.2002;
- ² R. Kienberger, M. Hentschel, M. Drescher, G. Tempea, C. Spielmann, G. Reider, P. Corkum, F. Krausz: Zeitaufgelöste Ionisationsdynamik im Bereich der Licht-Oszillationsperiode; 51. Jahrestagung der Österreichischen Physikalischen Gesellschaft, Wien; 17.09.2001 - 21.09.2001; in: ÖPG 2001; (2001), S. 170 - 171.
- ² R. Kienberger, M. Drescher, M. Hentschel, G. Tempea, C. Spielmann, G. Reider, P. Corkum, F. Krausz: Near-1-fs X-ray pulses: on the way to attosecond metrology; Poster: 2001 Gordon Research Conference on Nonlinear Optics and Lasers, New London, NH, USA; 29.07.2001 - 03.08.2001.
- ² M. Hentschel, M. Drescher, R. Kienberger, G. Tempea, C. Spielmann, G.A. Reider, P. Corkum, F. Krausz: Generation and measurement of single sub-laser-cycle XUV harmonic pulses; ATTO network meeting, Paris, Frankreich (**invited**); 25.01.2001 - 27.01.2001.
- ² M. Hentschel, R. Kienberger, M. Drescher, P. Corkum, F. Krausz: Toward Attosecond Metrology; The 2nd International Conf. on Superstrong Fields in Plasmas, Varenna (Lc), Italy (**invited**); 27.08.2001 - 01.09.2001; in: Programme and Abstracts; (2001), S. IM4.
- ² M. Hentschel, R. Kienberger, M. Drescher, G. Reider, C. Spielmann, F. Krausz: Erzeugung und Messung ultrakurzer Röntgenpulse; 51. Jahrestagung der Österreichischen Physikalischen Gesellschaft, Wien; 17.09.2001 - 21.09.2001; in: ÖPG 2001; (2001), S. 171 - 172.
- ² M. Hentschel, R. Kienberger, M. Drescher, G. Reider, C. Spielmann, F. Krausz: Ultrafast X-Ray Generation and its Application; The 14th Annual Meeting of the IEEE Lasers & Electro-Optics Society, La Jolla, San Diego, Cal., USA (**invited**); 11.11.2001 - 15.11.2001; in: 2001 IEEE/Leos Annual Meeting Conference Proceedings; (2001), S. 523 - 524.

- ² M. Hentschel, R. Kienberger, M. Drescher, G. Tempea, C. Spielmann, G.A. Reider, P. Corkum, F. Krausz: Near 1-fs X-Ray Pulses: On the Way to Attosecond Metrology; Poster: Seminar on Fundamentals of Laser Interactions III, K  htai, Tirol, Austria; 13.01.2002 - 18.01.2002.
- ² M. Hentschel, M. Schn  rer, R. Kienberger, C. Spielmann, F. Krausz, C. Strelt, P. Wobrauschek: Femtosecond X-ray   uorescence from light elements excited by laser harmonics; 12th International Conference on Ultrafast Phenomena, Charleston, South Carolina, USA; 09.07.2000 - 13.07.2000; in: The Twelfth International Conference on Ultrafast Phenomena; (2000), S. 15 - 16.
- ² M. Drescher, M. Hentschel, R. Kienberger, C. Spielmann, G.A. Reider, N. Milo-sevic, T. Brabec, U. Heinzmann, P. Corkum, F. Krausz: Isolated sub-femtosecond high harmonic pulses characterized by laser-  eld/XUV-intensiv cross-correlation; ATTO network meeting, Politecnico di Milano, Milano, Italy; 22.11.2001 - 24.11.2001.
- ² M. Drescher, M. Hentschel, R. Kienberger, G. Tempea, C. Spielmann, G. Reider, P. Corkum, F. Krausz: Measurement of near-attosecond XUV pulses by photoemission-cross-correlation; Intern. Workshop on Ultrafast Surface Dynamics, San Sebastian, Spanien; 09.07.2001 - 11.07.2001.
- ² M. Drescher, M. Hentschel, R. Kienberger, G. Tempea, C. Spielmann, G.A. Reider, P. Corkum, F. Krausz: Visible-EUV cross-correlation experiment resolving dynamics on the time scale of a single optical cycle; DPG Tagung, Berlin, Germany (**invited**); 02.04.2001 - 06.04.2001.
- ² M. Schn  rer, C. Strelt, P. Wobrauschek, M. Hentschel, R. Kienberger, C. Spielmann, F. Krausz: Femtosecond X-ray   uorescence from light elements excited by laser harmonics; CLEO/Europe'00, Nice, France; 10.09.2000 - 15.09.2000; in: 2000 Conference on Lasers and Electro-Optics Europe; (2000), S. 266.
- ² C. Spielmann, M. Drescher, M. Hentschel, R. Kienberger, G. Reider, F. Krausz, T. Guo: Lasergenerierte ultrakurze R  ntgenpulse; 51. Jahrestagung der   sterreichischen Physikalischen Gesellschaft, Wien (**invited**); 17.09.2001 - 21.09.2001; in:   PG 2001; (2001), S. 95.

- ² C. Spielmann, M. Drescher, M. Hentschel, R. Kienberger, G. Tempea, G.A. Reider, P. Corkum, F. Krausz: X-ray Pulses Approaching the Attosecond Frontier; Vth Femtochemistry Conference, Toledo, Spain (**invited**); 02.09.2001 - 06.09.2001; in: Book of Abstracts; (2001), S. 28.
- ² C. Spielmann, M. Schnürer, M. Hentschel, R. Kienberger, G. Tempea, A. Poppe, A. Apolonski, T. Brabec, F. Krausz: Generation and application of intense few cycle laser pulses; ULIA Euroconferences, Pisa, Italy (**invited**); 29.09.2000 - 03.10.2000; in: ULIA Euroconferences - 2; (2000), S. 91.
- ² C. Streltsov, M. Schnürer, M. Hentschel, R. Kienberger, C. Spielmann, F. Krausz, P. Wobrauschek: X-ray fluorescence analysis of low-z-elements induced by a femtosecond laser; Poster: 49th Annual Denver X-Ray Conference, Denver, Colorado, USA; 31.07.2000 - 04.08.2000; in: Abstracts; (2000), S. 102.
- ² P. Wobrauschek, M. Schnürer, M. Hentschel, R. Kienberger, C. Spielmann, F. Krausz, C. Streltsov: Femtosecond laser induced X-ray fluorescence analysis; Poster: European Conference on Energy Dispersive X-Ray Spectrometry, Krakow, Poland; 18.06.2000 - 23.06.2000; in: EDXRS-2000 University of Mining and Metallurgy; (2000), S. 58.
- ² P. Wobrauschek, M. Schnürer, M. Hentschel, R. Kienberger, C. Spielmann, F. Krausz, C. Streltsov: Röntgenfluoreszenzanalyse von leichten Elementen angeregt durch Femtosekunden Laser induzierte Röntgenstrahlung; Poster: 51. Jahrestagung der Österreichischen Physikalischen Gesellschaft, Wien; 17.09.2001 - 21.09.2001; in: ÖPG 2001; (2001), S. 52.

Contents

| | |
|---|-----------|
| Danksagung | i |
| Kurzfassung | ii |
| Summary | iv |
| 1 Motivation | 1 |
| 2 Generation of sub-femtosecond pulses | 4 |
| 2.1 The laser system | 5 |
| 2.2 High-order harmonic generation | 6 |
| 2.2.1 Principle | 7 |
| 2.2.2 Setup | 12 |
| 2.2.3 Spectrum | 15 |
| 2.2.4 Single attosecond pulses | 16 |
| 3 Measurement of sub-femtosecond pulses | 21 |
| 3.1 Cross-correlation between visible and XUV-pulses | 22 |
| 3.1.1 Principle | 24 |
| 3.1.2 Setup | 28 |
| 3.2 Detection and measurement | 33 |
| 3.2.1 Time of flight spectrometer | 33 |
| 3.2.2 Measuring procedure and acquisition of measurement data . . . | 37 |
| 3.3 Interpretation of the results | 40 |
| 3.3.1 Ab initio calculations: duration of isolated pulses | 40 |
| 3.3.2 Single pulses | 42 |

| | |
|---|-----------|
| 3.4 Expedited attosecond diagnosys | 45 |
| 4 Time-resolved attosecond spectroscopy | 52 |
| 4.1 Basic tools | 52 |
| 4.2 Experimental applications | 54 |
| 5 Conclusions and outlook | 58 |
| A HH intensity measurement device | 60 |
| B Control of wide-range piezo stage | 62 |
| C Routine to measure XUV-/VIS cross-correlation online | 64 |
| D Program for measuring cross-correlation scans | 66 |
| Bibliography | 68 |
| Curriculum vitae | 75 |
| Lebenslauf | 76 |

Chapter 1

Motivation

The insight in always smaller microscopic units of matter as well as in always shorter courses of chemical, physical or atomic processes give important information used for basic research. For example, knowledge of the dynamics of electrons and holes in semiconductor structures is the key for developing faster electronic devices. Or, at a more basic level, understanding what happens inside excited atoms by following the motions of the electrons is likely to impact future development of x-ray lasers. The interest in these ultrashort processes is the driving force behind the development of sources and measurement techniques that allow time-resolved studies at ever shorter timescales.

Femtosecond spectroscopy ($1 \text{ fs} = 10^{-15} \text{ s}$) has already now been a very powerful means of tracking changes in the nuclear structure of molecules, such as vibrations or the breaking and formation of chemical bonds, since the characteristic time scale for atomic motion on atomic length scale (0.1 nm) extends from a few femtoseconds to a few thousand femtoseconds [1, 2]. Time-domain access to a wide range of electron dynamics in the atomic shells, however, has been frustrated so far by the speed of electronic relaxation processes.

For example, the wave function of bound electrons, following an energetic excitation, e.g. ionization or the creation of an inner-shell vacancy, tends to evolve on an attosecond time scale. This can be seen at the most simple case, the electron of hydrogen, which - after being partially excited into the 2s-state - undertakes so called quantum beats, resulting in a breathing of the probability distribution of the electron (see Figure 1.1). Another important class of dynamics are inner-shell electronic transitions. Insight

into these processes could until now only be gained indirectly from frequency-domain measurements of transition linewidths [3] but not in the time domain.

In the classical scheme of time-resolved experiments, a short excitation pulse setting the process going and a short probe pulse for taking snapshots of subsequent stages of its evolution [4] constitute the basis for gaining experimental access to fast-evolving microscopic processes. For example, electrons inside atoms and molecules can be excited and subsequently relax within attoseconds to femtoseconds, interacting at different instants of time with sub-femtosecond pulses for capturing and reconstructing these ultrafast motions. The resolution of time-resolved measurements is limited by the exposure time, a fact, which is well known from photography, but acts as a big challenge on ultrashort timescale. To trace the processes mentioned above, it is evident, that sub-femtosecond pulses are required.

Nature, however, sets a limit to such pulses as they can be produced by laser light in the visible range. At a wavelength of 780 nm, for instance, one oscillation cycle lasts for 2.6 fs, setting a practical lower limit on the pulse-duration. Currently available laser pulse durations have closely approached this limit [5]-[10]. In order to reach even shorter pulse durations, one has to draw on shorter wavelengths in the XUV (extreme ultraviolet) respectively x-ray regime [11] - [14], which offer, owing to their short wave cycle, the potential for producing electromagnetic radiation of attosecond duration [15] - [18].

Most sources providing XUV or x-ray radiation - e.g. x-ray tubes or synchrotrons - do not have the potential of generating sub-femtosecond pulses for several reasons: lack of coherence between different wavelengths or occurrence of highly modulated line spectra, for instance. From this knowledge, it has to be concluded that only the process known as high-order harmonic generation (HHG) in atoms by femtosecond lasers can be used as a means for generating bursts of attosecond duration.

Moreover, the XUV fluences available from current high-harmonic sources are many orders of magnitude lower than required by XUV-pump/XUV-probe spectroscopy, while conventional schemes of visible-light/XUV cross correlation, yielding a convolution of the respective pulse envelopes, do not provide sub-fs time resolution. Using few-cycle visible laser pulses [19] for the generation of isolated soft-x-ray harmonic pulses [20] and a special geometry for detecting photoelectrons originating from atoms exposed simultaneously to both of these pulses, our work offers a way to overcome

these limitations. As any tool can only be used after having been characterized properly, a profound measurement of these sub-femtosecond pulses plays an important role. Unfortunately 'conventional' methods of measurement fail at those short wavelengths, auto-correlation for example, which will be pointed out later.

A cross-correlation measurement between the XUV- and the fundamental laser pulses has been proved to be a powerful method and will be addressed in Chapter 3. Previously, the generation of sub-femtosecond pulses by HHG will be described in the following Chapter 2.

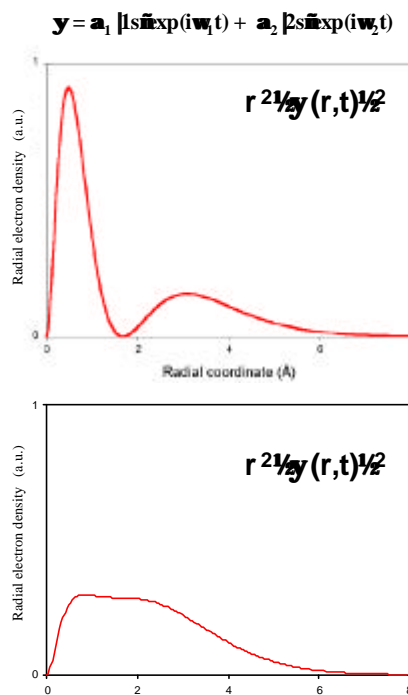


Figure 1.1: Probability distributions of an electron bound in the shells of a hydrogen atom at two different instants of time after having been excited, e.g. by an XUV pulse. The oscillatory movement occurs at a period of 400 as and is called quantum beat.

Chapter 2

Generation of sub-femtosecond pulses

Atomic spectroscopy is dependent on coherent extreme ultraviolet (XUV) and X-ray sources as they offer the potential for producing electromagnetic radiation of attosecond duration, owing to their short wave cycle.

High-order harmonics of femtosecond laser radiation [11, 14] was indicated [15] and recently shown [16] to produce trains of attosecond pulses in the extreme ultraviolet extending over some 10 fs. This time structure at ultrahigh (T_0^{-1} or $2T_0^{-1}$) repetition rates can result from the superposition of frequency-converted coherent radiation [21, 22, 23]. Most simply, pulse trains emerge by superimposing on the driving field its second and third harmonic but they are usually realized by selecting a number of harmonics over a substantial band near the highest photon energies (cut-off) from the high-harmonic spectrum consisting of narrow-band, discrete harmonics.

However, attosecond time-resolved measurements still appeared to be out of reach even after this achievement, because straightforward interpretation of spectroscopic data requires isolated, single pulses [17, 18], since the very short ($\gg 1$; 2 fs) pulse intervals within the train prevents an unambiguous interpretation of sampling.

Driving the high-order harmonic generation process by few-femtosecond laser pulses comprising just a few (typically < 3) wave cycles (within their full width at intensity half maximum) it has been predicted that - under certain conditions - it is possible to generate a single, isolated attosecond pulse (per laser pulse) burst. This technique has been developed and will be presented in the following sections.

2.1 The laser system

In our experiments coherent high-order harmonic generation (HHG) is accomplished by focusing 0.7-mJ linearly polarized \gg 780-nm center-wavelength laser pulses of 7 fs duration at a 1 kHz repetition rate [24] into a volume of Ne gas [25]. Principle, setup and results will be addressed in Section 2.2.

The pulses originate from a dispersion-controlled, Kerr-lens-modelocked Ti:sapphire oscillator delivering sub-10-fs pulses having a pulse energy of about 4 nJ at a repetition rate of approximately 80 MHz. After being temporally stretched by a 10-cm slab of SF57-glass these pulses are passed through a multipass Ti:sapphire amplifier in a confocal geometry. When pumped with \gg 10-mJ pulses at a 1 kHz repetition rate by a Q-switched, frequency doubled, lamp-pumped Nd:YLF laser, the amplifier boosts the pulse energy to typically 1.5-1.7 mJ in ten passes through the amplifier crystal, which magnifies the energy of one pulse by about 1 million times. Amplification is followed by recompression to a duration of typically 20-25 fs by two pairs of fused silica Brewster prisms. The compressor throughput is higher than 90% and results in a pulse energy of 1.3-1.5 mJ [26].

For further compression the pulses are focused into a hollow core fused silica fiber with an inner diameter of 250 μ m and a length of 1 m. The fiber is filled with neon at \gg 1 bar which imposes a dynamic phase shift on the pulse propagating down the waveguide due to the optical Kerr effect. The frequency broadening induced in this manner is converted into temporal compression by a set of broadband chirped dispersive mirrors yielding pulse durations down to 5-7 fs. The finally available pulse energy is typically 0.5-0.7 mJ, corresponding to a peak power of around 0.1 TW.

As will be pointed out in Section 2.2.4 and in Chapters 3 and 4 the laser system has three very important characteristics: (i) The achievable high intensity and (ii) the ultrashort, few-cycle pulse duration are an indispensable feature for the generation of sub-femtosecond pulses. Further on, few cycle pulses turned out to be essential for time-resolved attosecond spectroscopy. (iii) The high repetition rate of 1 kHz leads to practically useful XUV photon fluxes. Moreover, the detection system (see Section 3.2.1) prefers to handle 'few'-photoelectron events at high repetition rates than single events of a huge number of photoelectrons.

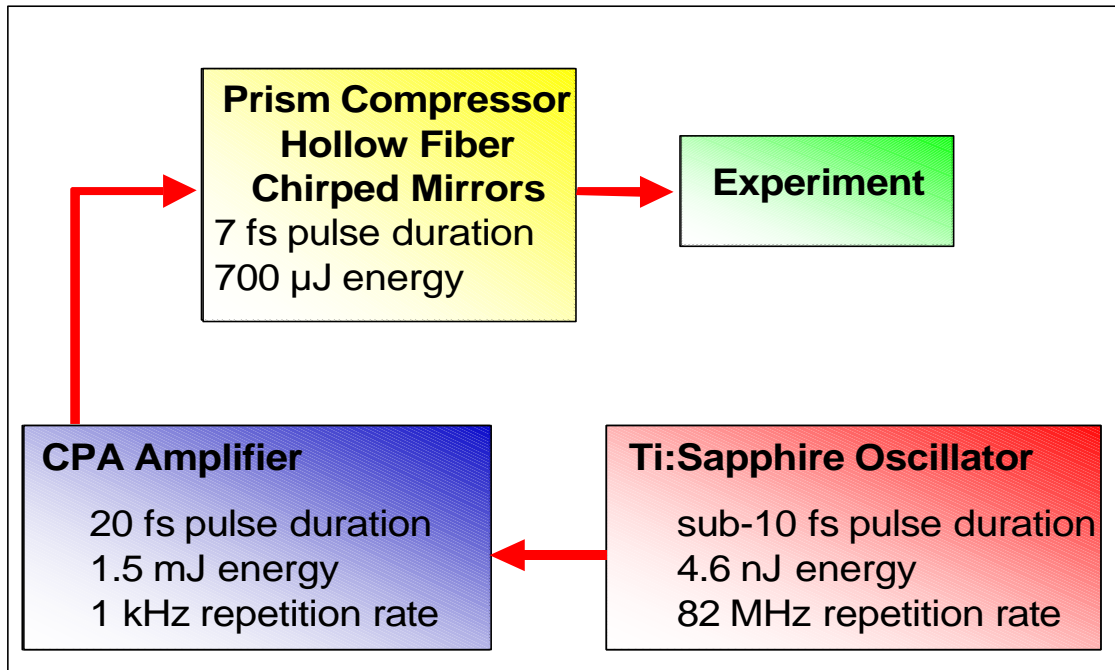


Figure 2.1: Block-diagram of the entire laser system showing all features and characteristics

2.2 High-order harmonic generation

Excellent coherence and relatively low pump-energy requirements, which can be provided by table-top laser systems, make HHG an attractive laboratory short-wavelength source. Using few-cycle pulses [19, 27, 28] for high-order harmonic generation [11, 14, 29] is ideal for the purpose of generating sub-femtosecond pulses. High-order harmonics are generated by electrons removed from an atom by a high laser field and then driven back to their ion of origin. This process is repeated quasi-periodically, each half cycle of the driving laser wave, resulting in a discrete frequency spectrum made up of high-order odd harmonics of the driving laser. The highest-order 'harmonics' are produced near the intensity peak of the laser pulse, as the recollision energy of the electrons is highest when the laser field is largest. Using a few-cycle driver and passing the harmonics through a filter that transmits only the highest frequencies, we select radiation produced only within a fraction of the laser cycle near the peak of the pulse. This method has been predicted to be capable of generating single XUV/x-ray pulses

of $\gg 100$ -attosecond duration emitted in a collimated, laser-like beam [18, 30, 31].

2.2.1 Principle

High-order harmonic generation is a process resulting from an interaction of electric field provided by laser pulses with atoms [11, 14, 32] - [41], atom clusters [42, 43] and molecules [44, 45]. High intensity, linearly polarization and ultrashort pulse duration are indispensable requirements for this sort of frequency transformation from the visible spectral range ($\gg 400$; 800 nm) into the XUV- or x-ray regime. If the pulses reach a duration of a few light field oscillation cycles, the highest-order harmonics merge to a continuum, as will be discussed in Section 2.2.4.

Interaction of the laser with a single atom

Although the process of HHG can be calculated and simulated by a quantum-mechanical model [57], which was done to evaluate the results presented in this thesis (see Section 3.3.1), it can be well understood by a semi-classical model [29, 46] based on two approximations first introduced by Keldysh for the calculation of strong-field ionization processes [3, 47].

- (i) After its liberation the electron is treated as a free particle by neglecting the effect of the Coulomb potential in positive-energy (continuum) states.
- (ii) The contribution of all other bound states except the ground state of the evolution of the system is neglected. This is fulfilled in the so-called non-perturbative regime, where $\gamma < 1$, with γ being the Keldysh parameter

$$\gamma = \frac{\omega_L \sqrt{2W_b}}{E_a}; \quad (2.1)$$

where W_b is the binding potential, ω_L is the laser frequency and E_a is the amplitude of the laser electrical field strength. Ultrashort, high intensity laser pulses focused to a small spot provide this non-perturbative regime. The emission of harmonic radiation from a single atom is determined by the dipole acceleration $(d^2/dt^2) \langle \mathbf{r}^a | \mathbf{j} | \mathbf{r}^a \rangle$, where the electron wavefunction ψ^a is the solution of the time-dependent Schrödinger equation in the presence of a driver laser field E_L [48, 49].

Under the two assumptions above, the quantum-mechanical expectation value of the atomic dipole moment responsible for HHG is obtained as a product of three probability amplitudes.

$$d(\omega) = \sum_{\omega_b} \frac{1}{P_j} a_{\text{ion}}(\omega_b) a_{\text{pr}}(\omega_b; \omega) a_{\text{rec}}(\omega) \quad (2.2)$$

The factors $a_{\text{ion}}(\omega_b)$, $a_{\text{pr}}(\omega_b; \omega)$ and $a_{\text{rec}}(\omega)$ represent the probabilities, that the three steps of the HHG, 'ionization', 'propagation' and 'recombination', as it can be regarded from the view of the semi-classical model, occur.

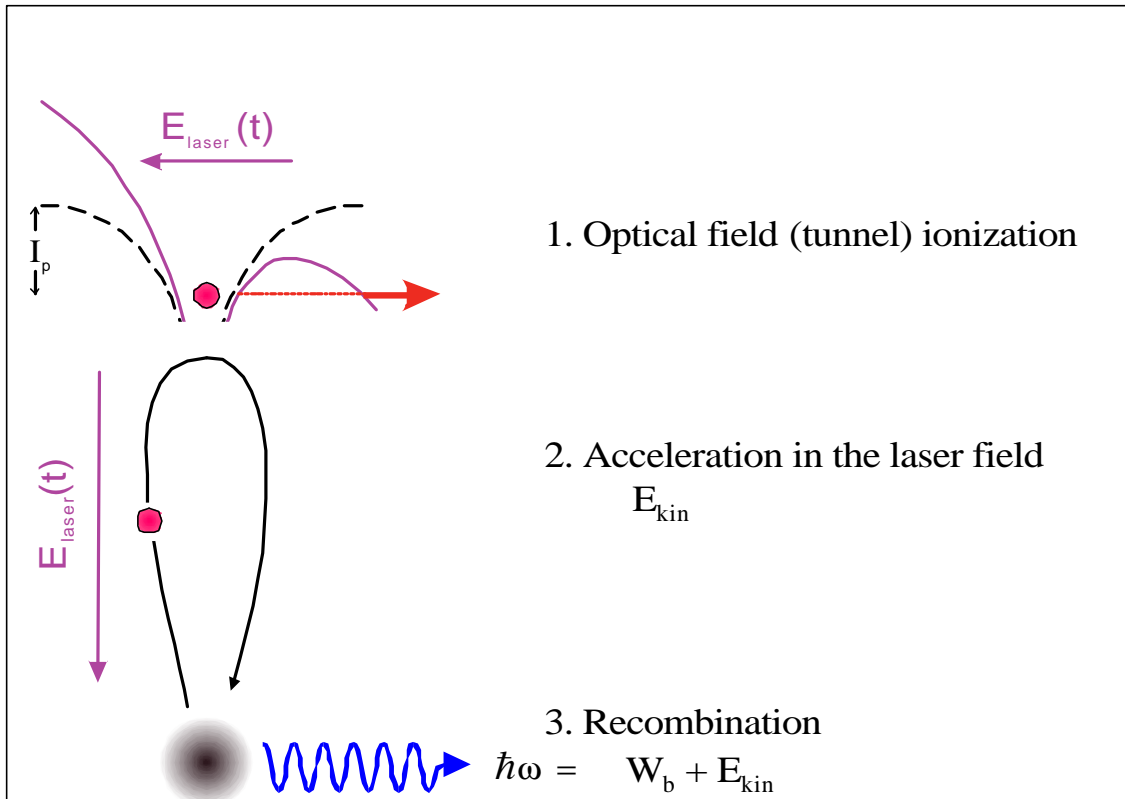


Figure 2.2: Principle of high-order harmonic generation in the framework of the semi-classical model described in the text.

These three steps are depicted in Figure 2.2:

(a) A free electron is 'born' at instant ω_b by tunnel ionization. This happens when the Coulomb potential of the atom is bent down so strongly by the laser electric field that the most weakly bound electron can tunnel through the finite barrier and is freed.

(b) The electron is accelerated by the laser electric field and moved apart from the ionized atom. When the laser field reverses its sign, the electron will start to slow down, come to rest and accelerate towards the ion. As Figure 2.3 shows, the trajectories highly depend on the time of 'birth' of the electron. In other words, only electrons set

free around a certain absolute phase $\varphi_0 = 17^\pm (\gg 0:1/4)$ of the carrier (cosine) oscillation (at ζ_b) have the possibility to return to the ion at instant ζ , which is represented by the possibility $a_{pr}(\zeta_b; \zeta)$.

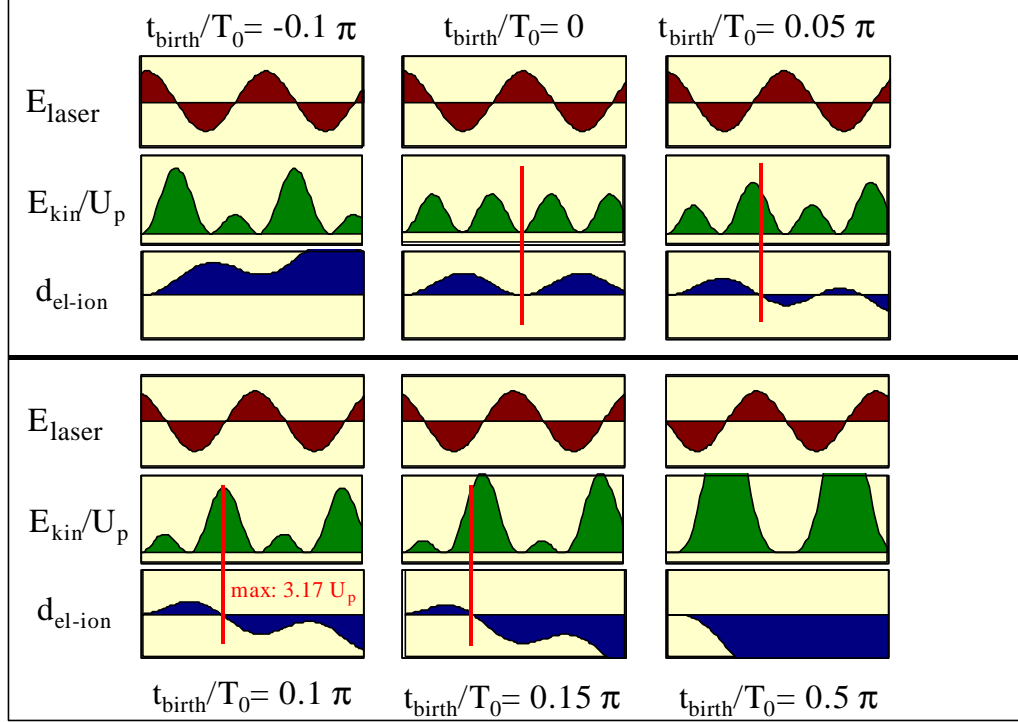


Figure 2.3: Different instants of 'birth' of the electron with respect to the laser electric field - depicted as the left margin of each chart - lead to different accelerations and therefore different trajectories. This can be seen at the electron coordinate over time, charted as the distance between the freed electron and the ion $d_{\text{el-ion}}$. Only if the instant of birth is around $\gg 0:1/4$ the electron can return to the ion, and before recombination an energy up to $3:17U_p$ can be integrated.

(c) With a certain probability $a_{\text{rec}}(\zeta)$ the electron hits the ion, and upon recombination into its ground state a photon is emitted with an energy of $\hbar\omega_x = W_b + E_{\text{kin}}(\zeta)$, where W_b is the binding energy. E_{kin} is the kinetic energy of the electron gained from the laser field. Its value is maximum,

$$[E_{\text{kin}}(\zeta)]_{\text{max}} = 3:17 U_p(\zeta); \quad (2.3)$$

if the electron is born at a phase of 17^\pm after the oscillation peak of the laser electric field. The ponderomotive potential U_p is the cycle-averaged kinetic energy of a wiggling electron in the laser field and is given by

$$U_p(t) = \frac{e^2 E_a^2(t)}{4 m_0^2}; \quad (2.4)$$

with e and m being the charge and mass of the electron and with ω_0 and E_a the frequency and amplitude of the laser field. The factor 3.17 is achieved by the borders of integration from ζ_b to $\zeta = 0$. The highest photon energy obtainable, the so-called cut-off[®], is ultimately limited by the peak intensity of the laser pulse, i.e. $E_c = W_b + 3.17 U_p(0)$. In our experiments this is about 60 times the energy of the laser photons. Harmonics below the cut-off[®] can be generated at several quasi-periodic time instants within the driver pulse resulting in a spectrum of discrete odd harmonics of the laser frequency ω_0 . In the cut-off[®] region of a few-cycle laser pulse however, photons are generated only within one half cycle and give rise to a continuous spectrum.

It is evident that linear polarization is highly required at step (c), since any transverse component of acceleration would prohibit a recollision of the electron with the ion and set $a_{\text{rec}}(\zeta) = 0$.

Propagation and ensemble effects

Single-atom theory makes many important features of HHG understandable but a detailed comparison with experiments calls for a macroscopic theory including propagation and ensemble effects [50, 51]. There are three important propagation effects, namely (i) dephasing, (ii) absorption, and (iii) defocusing, setting a limit to the maximum achievable harmonic yield rate.

(i) The difference between the phase velocities of the driving laser field and the high harmonic wave results in a phase mismatch between partial harmonic waves emitted at $z=0$ and $z > 0$ in the gas medium. Since the index of refraction is almost unity for XUV wavelengths, the phase of the generated harmonic radiation is hardly influenced. The driving laser field, on the other hand, feels three components of dephasing.

(a) The so called Guoy phase shift is a simple geometric effect occurring at the focusing of a laser beam where the wave front undergoes a transition from a negative radius of curvature over a plane front to a positive radius of curvature. Due to this geometrical effect the coherent copropagation of fundamental (ω_0) and N^{th} harmonic field is limited to the coherence length

$$L_g = \frac{1/4 z_0}{N} = \frac{1/4^2 w_0^2}{N \omega_0}, \quad (2.5)$$

where z_0 is the Rayleigh range and w_0 the radius of the laser beam waist [50]. The coherence length is defined as the propagation length, at which the phase mismatch

between harmonic and fundamental radiation reaches $\frac{1}{4}$

(b) Ionization is one of the basic processes of HHG. As the process is very selective and the probabilities for right trajectories and recombination $a_{pr}(\omega_b; \omega) \ll a_{rec}(\omega)$ is far below 1 (photon conversion efficiency $\cdot 10^{-6}$), much more atoms are ionized leading to more free electrons than contribute to HHG. These electrons cause a refractive index less than 1, resulting in a dephasing length

$$L_{fe} = \frac{2 \frac{1}{2} c \epsilon_0}{N \omega_p^2(\omega_b)} \quad (2.6)$$

with the plasma frequency

$$\omega_p(\omega) = \frac{\sqrt{e^2 n_e(\omega)}}{m^2_0} \quad (2.7)$$

and the instantaneous electron density $n_e(\omega)$ [31]. If the positive refractive index of the neutral gas can be balanced with the contributions (a) and (b), e.g. by adjusting the pressure of the gas target properly, an equal speed of propagation is ensured for the harmonic and the driving field (within a certain spectral width).

(c) The single-atom dipole moment for HHG depends on the pulse intensity. As intensity changes during propagation due to diffraction, the phase of the dipole moment decreases, leading also to dephasing which is, at our setup, neglectible.

(ii) Due to its high photon energy, harmonic radiation can excite core electron states during propagation in the gas and be reabsorbed [3]. The conversion will saturate after the absorption length $L_{abs} = 1/\sigma n$ where σ is the ionization cross section and n is the gas density [60].

(iii) Defocusing is obtained by a free-electron profile created by the laser pulse during HHG, where the largest density is at the pulse peak and goes to zero at the pulse wings. Such a profile reduces the laser pulse intensity, leading to a limitation on the effective interaction length over which a particular harmonic can be generated. Compared to others, this effect usually plays a minor role.

As can be seen in the experimental results presented in Section 3.3, dispersion leads to a lengthening of the laser pulse, which can cause a reduced efficiency in the cut-off region. The change in the refractive index of the ionized gas leads to an instantaneous

frequency upshift of the driving pulse. This effect, which is also predicted by theory, does not cause any difficulties but rather benefits XUV-pulse characterization (see Section 3.3.2).

Finding optimum parameters for HHG

Limitations arising from geometric effects, such as dephasing by the Gouy shift and defocusing, depend on the confocal parameter and therefore can always be suppressed by increasing the pulse energy and the beam radius such that the peak intensity remains constant. In neon, conclusive evidence for the limiting role of absorption in few-cycle-driven HHG at the border of the XUV/soft x-ray regime has been obtained in previous studies [25]. Owing to the steep front edge of the few-cycle driver, harmonics up to the 100-eV photon energy range can be produced at fractional ionization levels as low as $n_e(z)/n_a = 0.5\%$, $n_e(z)$ being the electron- and n_a being the atom density. This results in a coherence length L_{fe} according to Eq. 2.6 that exceeds the XUV absorption length. At these low ionization levels and for sufficient large laser focus diameters, the phase advance of the driving laser induced by free electrons and the Guoy phase shift, which limit the coherence length, can be compensated by the phase delay caused by the positive contribution of the neutral atoms to the refractive index. This compensation, which can be optimized by fine adjustment of the density n_a (i.e. pressure) of the atomic gas, results in a substantial enhancement of the coherence length over a limited fraction of the interaction time.

Further on, the choice of the right radius of curvature of the focusing mirror, the diameter of the incoming beam, both influencing the focal spot diameter, and the z-position of the gas-target in relation to the focus influence highly the spectral efficiency of the conversion process. The optimum parameter set is described in the next section.

2.2.2 Setup

For the process of HHG, the laser pulses carried at $\lambda_L \gg 780 \text{ nm}$ ($\hbar\omega_L \approx 1.6 \text{ eV}$) with a duration of 7 fs and pulse energy of 0.5 mJ delivered at a repetition rate of 1 kHz [24] are focused into a vacuum chamber through an 0.3-mm-thick fused silica window.

The silver-coated spherical mirror provides a focal spot diameter of 120 to 150 μm ($\gg 3 \text{ mm}$ confocal parameter) by a radius of curvature of 800 or 1000 mm, respectively. The choice of the mirror as well as the position and packing pressure of the gas target

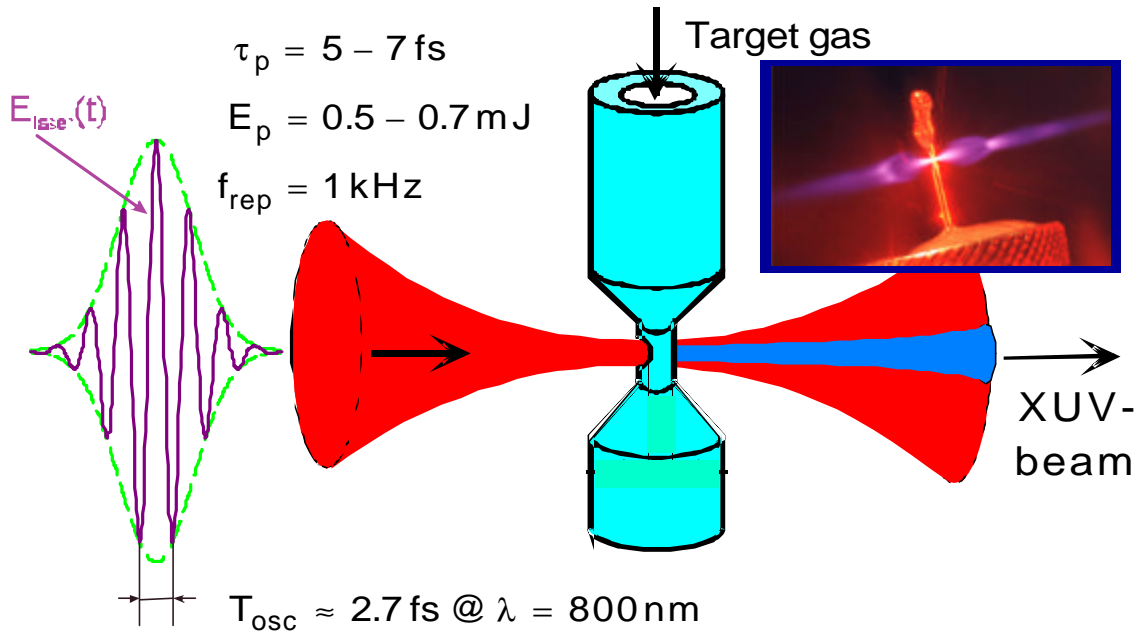


Figure 2.4: The focused 7-fs laser beam fights its way through the walls of a metallic tube (diameter $\gg 3$ mm) by ablation and interacts with neon atoms inside the tube to produce high-order harmonic radiation. The angle of divergence of the exiting harmonic beam ($\gg 0.7$ mrad in the near-cuto[®] region) is much lower than the one of the outgoing fundamental laser beam. The ionizing gas e[®]using from the tube can be traced owing to its uorescence emission (see photograph).

(see below) is important to fulfill the phasematching-condition described in Section 2.2.1. Near the focus of the beam, neon atoms e[®]using from holes drilled into a Ne-backed Ni-tube by the focused laser beam are exposed to peak electric fields of $\gg 8.8 \times 10^{14}$ W/cm² over an e[®]ective interaction length of $\gg 3$ mm. This interaction length can be tuned to achieve phase matching (see previous section) by squeezing the tube down to $\gg 1$ mm. They emit coherent soft-x-ray harmonic radiation up to photon energies exceeding 100 eV [25, 27]. Maximum yield at 90 eV photon energy is achieved at a backing pressure of 0.2 bar, which seems to be the optimum tuning as far as absorption is concerned. The chamber is pumped by a root pump to keep the background pressure in the range of $10^{i 2}$ mbar.

The XUV photons are delivered in a well-collimated beam having a divergence angle of $\gg 0.7$ mrad in the near-cuto[®] region. The conversion e[±]ciency at $\gg 90$ eV photon

energy / \gg 13 nm wavelength is about 10^{16} , providing about 10^7 photons/pulse in this region. As the profile of the focused fundamental laser beam is Gaussian-like, cut-off harmonics are only generated in the central part of the focus. In order to increase conversion efficiency over the whole focal area work on a profile tailoring towards a flat-top focal profile is in progress.

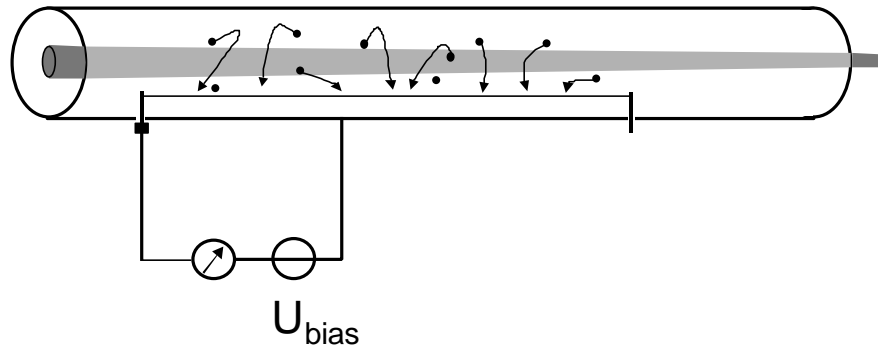


Figure 2.5: Schematic of the HH monitoring device and the principle of measurement.

A beamline connecting the generation- with the measurement chamber is pumped by a 330 l/s turbo molecular pump and separated by an aperture and a Zr-filter from the two chambers, respectively. The beamline tube contains a monitoring device for estimating the total harmonic flux (Fig. 2.5). It consists of an uninsulated wire taut 1 m along the tube wall biased with $U_{\text{bias}} \approx -2$ V. The positively charged residual gas particles ionized by the harmonic pulses are collected by the wire leading to a current. As ionization is a part of the 3-step HHG process, it is an indication of the harmonic radiation yield. This current is preamplified by a current/voltage converter and displayed on a computer, enabling to monitor the harmonic yield during measurements. Although this measurement is not wavelength selective, it provides important indications about the condition of the source and changes during experiments.

Appendix A shows the program for this measurement device realized by the measurement software package LabVIEW. A description of the subsequent measurement chain can be found in Section 3.1.2.

2.2.3 Spectrum

Driven with sub-100-fs laser pulses, high-order harmonic radiation typically lasts a few tens of femtoseconds [53, 54] and exhibits a quasi-periodic sub-structure of attosecond spikes at the highest (cut-off) harmonic photon energies [15, 16]. The spectrum of this radiation consists of discrete lines at odd multiples of the laser frequency, as a spectral manifestation of temporal periodicity with a period of $T_0=2$. In the absence of a significant frequency dependence of the spectral phase, the overall emission time is related to the linewidth of the individual harmonics, whereas the duration of individual spikes is determined by the overall spectral width of lines filtered out of the harmonic spectrum. The cut-off harmonics of a few-cycle light pulse were predicted to merge into a continuum, forming an isolated sub-femtosecond pulse [6, 18, 31, 55].

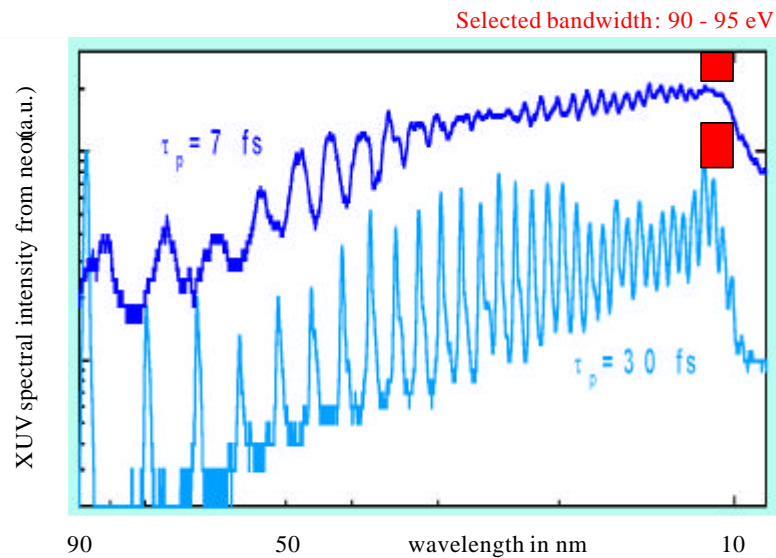


Figure 2.6: Spectra produced by multi-cycle (30 fs) and few-cycle (7 fs) 780 nm laser pulses. The highly modulated region near the cut-off in the first case merges to a quasi-continuum in the case of few-cycle pulses.

Figure 2.6 shows two different spectra produced by multi-cycle (30 fs) and a few-cycle (7 fs) 780 nm laser pulses. The highly modulated region near the cut-off turns into a quasi-continuum in the case of few-cycle driver pulses. This can be seen even more clearly, if a certain bandwidth in this region is selected by a bandpass filter, e.g. by a mirror determined by its reflectivity. The reasons and the consequences will be discussed in the next section, 2.2.4.

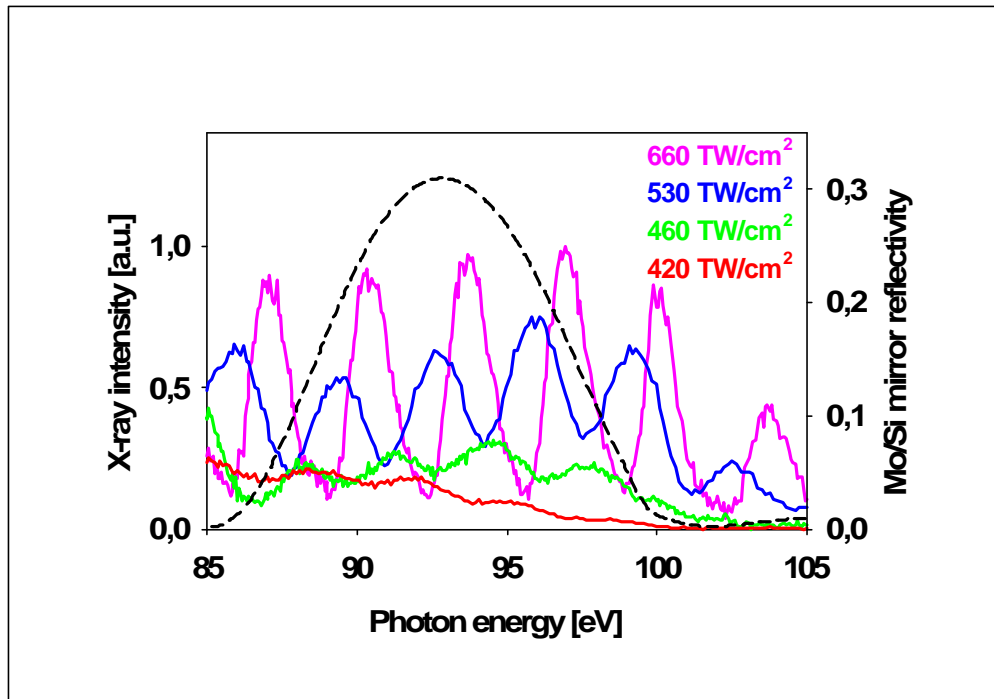


Figure 2.7: High-order harmonic spectra emitted from a 2-mm-long, 110-mbar neon gas source exposed to linearly-polarized 7-fs, 780-nm laser pulses with peak intensities given in the figure. The degree of modulation at a certain wavelength range can be tuned by the intensity of the fundamental pulses.

As the cut-off[®] of the HHG process sensitively depends on the fundamental laser intensity, controlling the intensity e.g. by an iris (as it was done in the experiment), adjusts the position of the cut-off[®]. In this way the cut-off[®] region and - in the case of a few-cycle pulse - the quasi continuum can be shifted relatively to a bandpass filter. Figure 2.7 shows the resulting deeply modulated respectively flat spectra at the background of the spectral reflectivity of a multi-layer XUV mirror, acting as a bandpass filter.

2.2.4 Single attosecond pulses

In the time domain, harmonic radiation from HHG at a limited frequency band near the cut-off[®] is confined to a small fraction of $T_0=2$ within one laser oscillation period. In general, this results in a train of sub-femtosecond or even attosecond bursts of short-

wavelength radiation [22, 56]. Although the conversion efficiency of HHG is lower than that of other schemes for attosecond pulse generation [23], the advantage is that there exist several possibilities for cutting a single sub-femtosecond pulse out of the pulse train. One straightforward method is using few-cycle fundamental pulses. Under these conditions, emission of the high-energy end of the harmonic spectrum (near cut-off region) can be confined to one half-oscillation period near the pulse peak. By selecting a well-defined bandwidth near the spectral cut-off it is possible to filter out one single sub-femtosecond burst. Figure 2.8 shows the importance of few-cycle pulses used for this method in comparison with multi-cycle pulses, as well as the sensitivity of this tuning to the absolute phase ϕ (carrier-envelope phase) of the fundamental laser pulse. ϕ is defined over the laser electric field equation

$$E_L = E_a(t) \cos(\omega_L t + \phi): \quad (2.8)$$

Only 'cosine' pulses have the potential of producing single bursts. Within a pre-selected frequency band the fundamental pulse intensity is tuned in a way that only contributions by pulses having an absolute phase $\phi_0 = 0$ or $\phi_0 = \pi/4$ are selected (see Fig. 2.8).

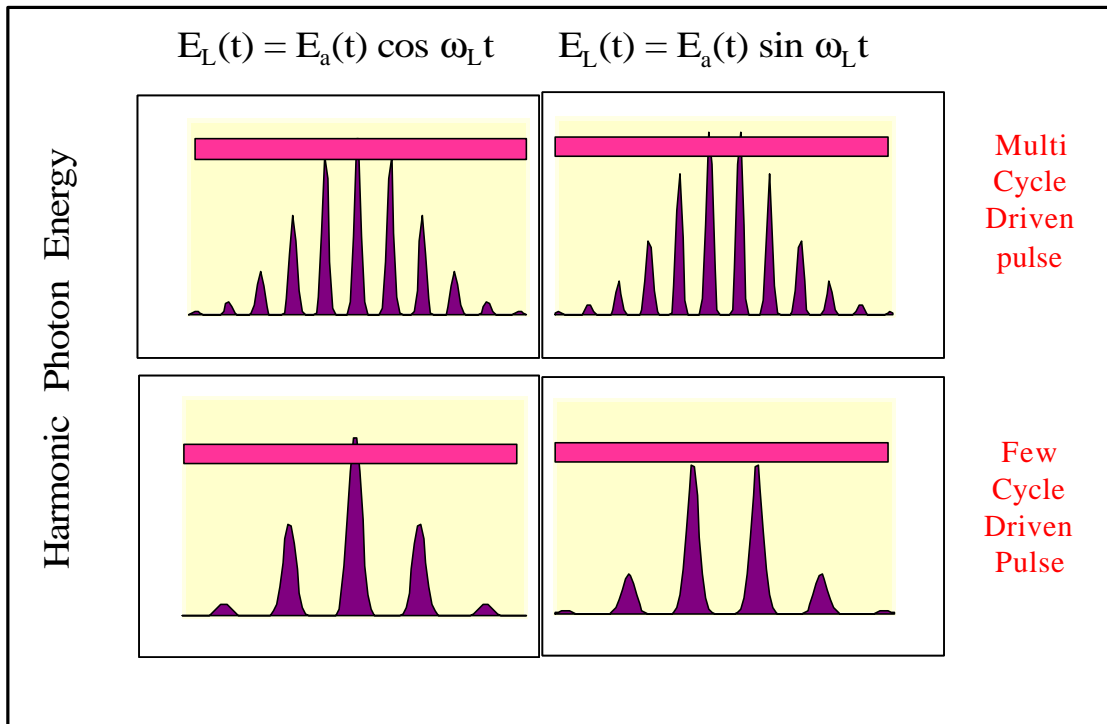


Figure 2.8: Comparison of HHG XUV-pulses generated by multi-cycle or few-cycle pulses in the case of different carrier phase delays in the time domain. If the spectral harmonic yield is carefully tuned towards a certain frequency band, single bursts can be selected.

Fig. 2.9 shows the difference of XUV bursts generated by sine respectively cosine pulses, namely the occurrence of a pulse train or a single burst. The difference in the overall duration of the emission is evident. Different results at a correlation with the driving laser field, represented by the red line, can be estimated (see Section 3.3.2).

The emergence of a single sub-femtosecond pulse from high-order harmonic generation in the few-cycle regime as realized in our experiment was corroborated by preliminary numerical studies based on a computer code [57] solving Maxwell's wave equations in three dimensions and calculating the radiation of the strongly-driven atomic dipoles using the quantum theory of Lewenstein et al [29]. These numerical calculations predict a near bandwidth-limited isolated 530-as XUV pulse emitted from the neon high-harmonic source within the spectral range of 90 eV \leq 2.5 eV under our experimental conditions (see Fig. 2.10a). They also indicate the potential for even shorter pulses, if the XUV mirror bandwidth defining the above spectral range is in-

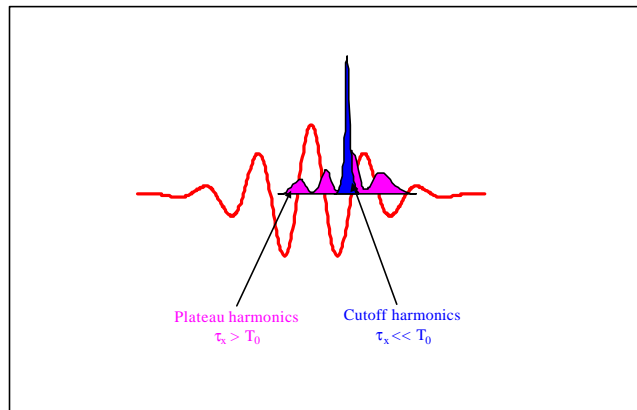


Figure 2.9: Comparison of HHG XUV-pulses generated by sine respectively cosine pulses.

creased. In fact, increasing the XUV mirror bandwidth by factor of 2 in our simulations results in an 330-as XUV pulse, accompanied by somewhat more pronounced satellites (Fig. 2.10b).

Section 3.3.2 will reveal a good agreement between experimental data and these theoretical predictions.

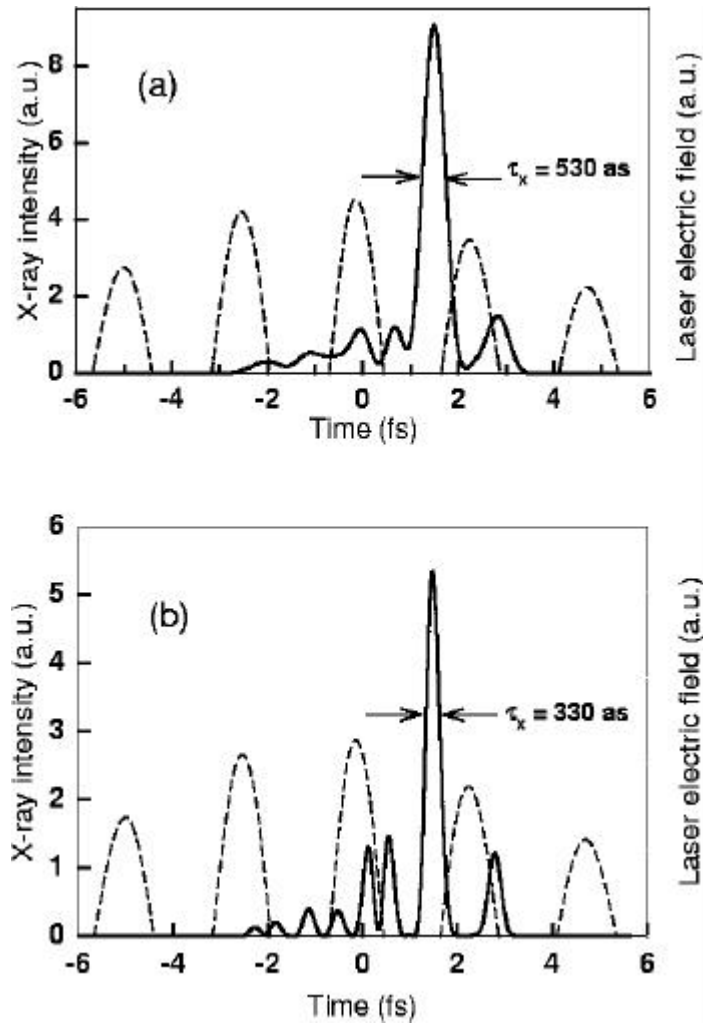


Figure 2.10: Calculated far-field, near-axis temporal intensity profile of XUV harmonic radiation (full line) selected within the spectral range of (a) $90 \text{ \AA} \pm 2.5 \text{ eV}$ and (b) $90 \text{ \AA} \pm 5 \text{ eV}$, produced in a 3-mm-long 200-mbar neon gas volume by a 7-fs, 780-nm Gaussian laser pulse $E(t) \propto \exp(-t^2/\tau_L^2) \cos(\omega_0 t + \phi)$ with $\phi = 0$ (cosine pulse) and an on-axis peak intensity of $8 \times 10^{14} \text{ W/cm}^2$. The dashed line shows the on-axis electric field of the laser pulse exiting the interaction region.

Chapter 3

Measurement of sub-femtosecond pulses

The most direct information about the duration of short °ashes of electromagnetic radiation can be gained from time-domain measurements [58, 59]. To this end, the burst to be characterized must be probed by a sampling pulse that is comparable to or shorter than the duration of the burst. In the optical regime this concept has been implemented by nonlinear auto-correlation techniques. Auto-correlation requires that the pulse is split into two replica pulses, and then recombined in a nonlinear medium where the nonlinear process is sensitive to their temporal overlap. Because of the unfavourable scaling of the nonlinear polarizability with matter and the low energy of the XUV pulse to be measured, these techniques can currently not be applied to radiation at wavelengths much shorter than 100 nm [53]. Thus, although auto-correlation is conceptually simple and well understood, so far it has been impossible to implement in the XUV regime.

Recently an interesting variation of this concept by splitting the driving pulse rather than the harmonic pulse has been proposed [15]. The idea is that the ionizing gas which produces the harmonics can also be used as the nonlinear medium to measure their duration [60]. An attosecond sub-structure is observed on a much longer (> 10 fs) auto-correlation feature. However, although this approach is experimentally simple, it is conceptually complex since production and measurement are intertwined. The detected signal can be regarded as a high-order auto-correlation of the driver laser pulse. The extent to which this provides insight into the temporal structure of the

generated high harmonics (auto-correlation signal) is not quite clear at present.

The only alternative for characterizing sub-femtosecond XUV/x-ray pulses is to correlate the short-wavelength burst with the electric field evolution of a strong visible or near-infrared laser pulse in a cross-correlation scheme, where the quarter wave cycle provides an attosecond probe for sampling the XUV/x-ray pulse. To exploit the potential of the above described technique for measuring XUV bursts with high temporal resolution, jitter between the XUV pulse and the laser pulse probing the XUVs needs to be minimized. This requirement can be most efficiently fulfilled by using the same laser pulse for generation and measurement, which becomes feasible owing to the low levels of ionization at which few-cycle drivers are able to efficiently generate harmonics up to the 100-eV region [25]. As a result, an enhanced conversion efficiency is combined with a nearly undistorted propagation of the laser pulse through the weakly ionizing harmonic source. This enables us to record high-resolution cross-correlations with the co-propagating, perfectly synchronized harmonic pulse by employing a compact, highly stable delay stage.

The key to the progress reported in this work is a novel measurement technique. It allows measuring the duration of broad-band ($> \hbar\omega_L$) XUV pulses with sub-laser-cycle resolution. The method is intuitive, can be generalized to a wide range of XUV wavelengths, and offers sub-femtosecond resolution. Using this technique, we have measured a duration of 650 as of isolated 90-eV XUV pulses generated from our 7-fs-laser-driven high-harmonic source.

3.1 Cross-correlation between visible and XUV-pulses

The temporal characterization of the generated broadband (multi-eV-bandwidth) XUV/soft-x-ray pulses produced by HHG-sources turns out to be a formidable challenge, since conventional auto-correlation schemes based upon second order nonlinearities require photon fluences orders of magnitude higher than those available from existing HHG-sources. Here a novel cross-correlation technique will be proposed and demonstrated based on XUV photoionization in the presence of an intense few-cycle laser field [20, 61]. It is based on the effect that the final kinetic energy of XUV-generated photoelectrons is controlled by the oscillating light field at the instant of

ionization. The features (width and position) of the resulting photoelectron spectra as a function of the relative delay between XUV- and laser pulse are determined by a convolution of the laser light field and the XUV pulse envelope. Careful deconvolution allows to determine the duration of the XUV pulse and its timing jitter with respect to the light field on an attosecond time scale.

The experimental realization of this technique falls within a class of experiments that began with the work of Schins and co-workers [54, 62, 63, 64, 65]. Here the XUV pulse is 'cross correlated' against a short visible pulse. An XUV photon excites a bound atomic electron into a positive-energy state in the presence of a laser field. Laser-induced transitions from this state or a laser-induced shift in its energy (Stark shift) provide the nonlinearity linking the XUV to the laser pulse, enabling us to compare the XUV pulse duration with that of the visible pulse. In the experiments reported so far, a number of laser photons increasing rapidly with the laser intensity is absorbed and emitted by the freed electron (forced to oscillate at ω_L). To identify the Stark shift amidst the resulting sidebands in the photoelectron energy spectrum, or measure the amplitude of the sidebands the XUV spectral width must be kept significantly below the laser photon energy $\hbar\omega_L \approx 1.6$ eV to avoid overlap of the sidebands with the main peak. Without modification, Schins' approach cannot be extended to sub-laser-cycle XUV pulses for two reasons: (i) If we are to measure XUV pulses with durations of $\tau_x < T_0$, the photoelectron energy distribution must become broader than the laser photon energy, so that it is no longer possible to identify individual sidebands and measure their amplitudes or determine the Stark shift. (ii) If Stark shift shall become measurable in spite of the smearing of the photoelectron energy distribution, the laser field has to be increased, as ponderomotive energy tends to be dominantly supplied by the laser field. Because this is returned to the field as the laser pulse turns on there is no net contribution to the Stark-shift, which therefore saturates for increasing intensities.

In our experiments we show that choosing the geometry of observation carefully and confining the (dressing) laser field to a few oscillation cycles opens the door to broadband ($> \hbar\omega_L$) XUV pulse measurement with sub-femtosecond resolution. To this end, photoelectrons from atoms exposed simultaneously to a strong light field and an XUV pulse are detected with a time-of-flight (TOF)-spectrometer. The detection cone is aligned orthogonally to the electric field vector of the linearly polarized laser

field, in order to suppress a background in the photoelectron spectrum originating from above-threshold ionization (ATI) of the atoms by the laser. In the strong field limit, a quasi-classical model summarized in the following section gives proper account for the modifications of the photoelectron spectrum by the laser field.

3.1.1 Principle

Our method of measuring a cross-correlation between an XUV pulse and a visible laser pulse can be summarized as laser-light-assisted XUV photoionization. The basic idea is to overlap the two pulses with variable delay with respect to each other in a gas medium and measuring, as a function of delay, the kinetic energy of the photoelectrons stripped from the atoms by the XUV pulse.

The effect of a light field on the XUV photoelectron energy spectrum is now well understood within a quantum mechanical framework [66, 67]. In the strong field limit, the most conspicuous features can also be accounted for by a quasi-classical model treating the interaction as a two-step process [20]. According to this model, the photoelectron is first ejected by a short XUV pulse with a distribution of initial momenta known from conventional photoionization studies [3]. Subsequently, it is accelerated (or decelerated) by the light field. For XUV pulse durations τ_x very short as compared to $T_0=2\pi/\omega$, the model predicts that depending on the oscillation phase of the light field at the instant of 'birth' of the electron, a momentum component along the electric field vector is added to the initial momentum of the electron, resulting in a shift of the photoelectron angular distribution up or down in momentum space (Fig. 3.1). The momentum transferred from the light field is largest if the electric field of the light pulse is zero, i.e. its slope is maximum, at the instant of birth of the photoelectron. The width of the XUV photoelectron energy spectrum ΔW , which is equal to the bandwidth of the XUV pulse spectrum in the absence of the light field, increases with increasing momentum shift.

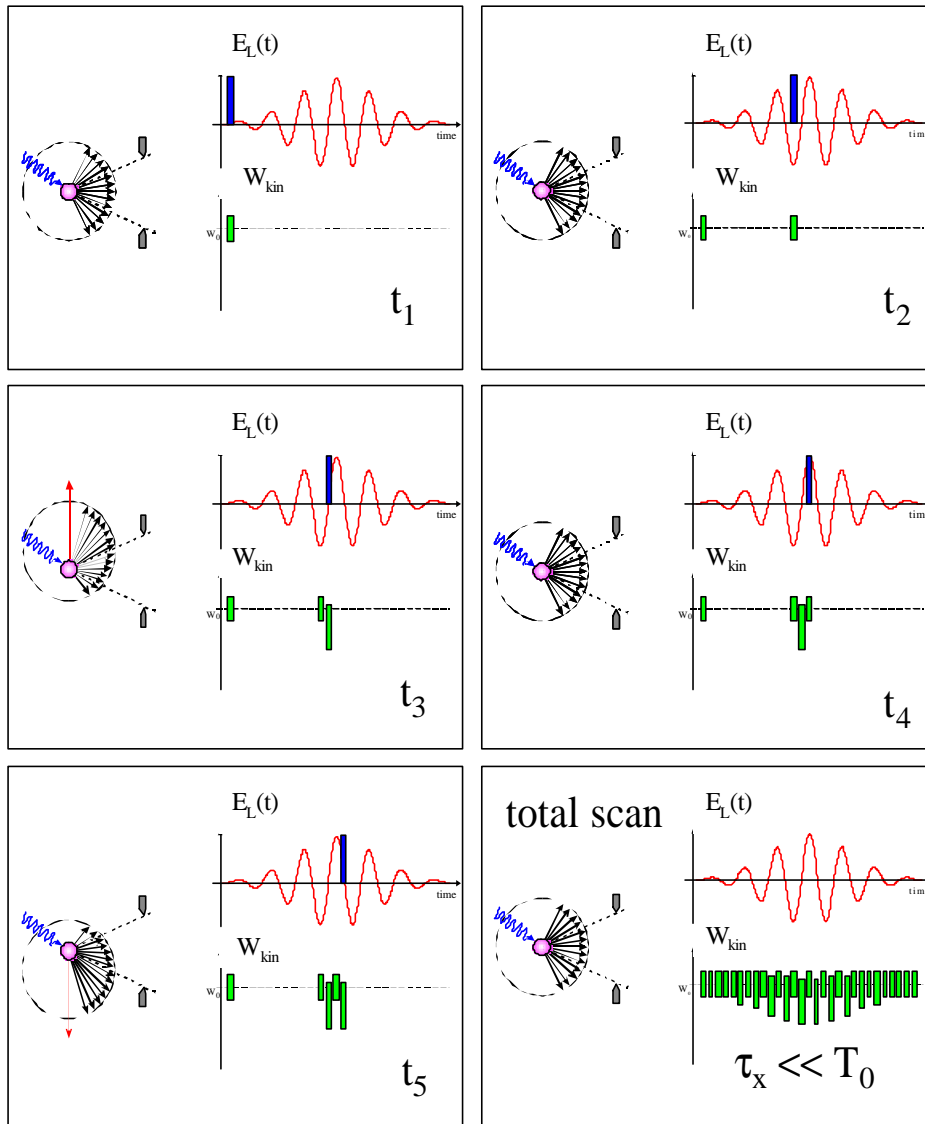


Figure 3.1: Principle of measuring light-field/XUV-intensity cross-correlation with attosecond resolution. The photoelectrons created initially with isotropic momentum distribution by the absorption of XUV photons pick up a momentum from the strong laser light-field. The light-induced momentum change $\langle p_x \rangle$ deforms the initial photoelectron momentum distribution at instants t_1 , t_2 , $t_3 = t_2 + T_0 = 4$, $t_4 = t_2 + 2T_0 = 2$, and $t_5 = t_2 + 3T_0 = 4$ as shown, where $E_L(t_3) = E_L(t_5) = 0$. Photoelectrons detected within a cone aligned orthogonally to the direction of the light-field vector (x direction) display a kinetic energy spread at t_3 and t_5 whilst remaining unaffected by the light-field at t_1 , t_2 and t_4 . The total scan shows the expected modulation of the spectra if $\tau_x \ll T_0 = 2$.

As the analysis in the next section will show, scanning the instant of birth of the photoelectron through the light field oscillations by changing the relative delay t_d between the light pulse and XUV pulse results in a modulation of the center of gravity as well as the width $\Delta W(t_d)$ of the XUV photoelectron spectrum with a period equal to one half of the light oscillation period T_0 . For sub-femtosecond XUV pulse measurement we shall exploit the field-induced spectral broadening [61] because this effect is enhanced by increasing the detection aperture as revealed by Fig. 3.1, resulting in a significantly enhanced signal yield and modulation amplitude of $\Delta W(t_d)$. By contrast, a modulation in the kinetic energy shift gets increasingly washed out with increasing detection angle, deteriorating the temporal resolution.

Taking advantage of the semi-classical approach outlined above, the motion of an XUV-induced photoelectron 'born' at a delay time t_d with respect to the peak of the laser pulse is governed by the classical equation of motion. Along the direction of laser polarization (x) this equation reads as

$$m\dot{v}_k = qE_L = \int eE_a(t) \cos \mu_L t; \quad (3.1)$$

where m and $\int e$ are the electron mass and charge, and $E_a(t)$ represents the amplitude envelope of the light pulse. In the adiabatic limit ($dE_a(t)/dt \ll E_a(t)\omega_L$) (which is a remarkably good approximation even for 7-fs pulses) the femtosecond laser pulse changes the velocity of the electron by

$$\Delta v_k = \frac{e}{m} \frac{E_a(t_d) \sin \mu_L t_d}{\omega_L} = \frac{\sqrt{4U_p(t_d)}}{m} \sin \mu_L t_d; \quad (3.2)$$

$$\Delta v_{\perp} = 0 \quad (3.3)$$

in the directions parallel and perpendicular to the laser polarization, respectively. Here

$$U_p = \frac{e^2 E_a^2(t_d)}{4m\omega_L^2} \quad (3.4)$$

is the electrons wiggling energy averaged over an optical cycle. This change of the initial velocity of the electron results in a modification of the final kinetic energy W_f . For $U_p \ll W_0$ the final energy is as given by

$$W_f \approx \frac{1}{4} W_0 + 2U_p(t_d) \sin^2 \mu_L t_d \cos 2\mu \\ + \frac{1}{8} \frac{U_p^2(t_d)}{W_0} \sin^2 \mu_L t_d \cos \mu; \quad (3.5)$$

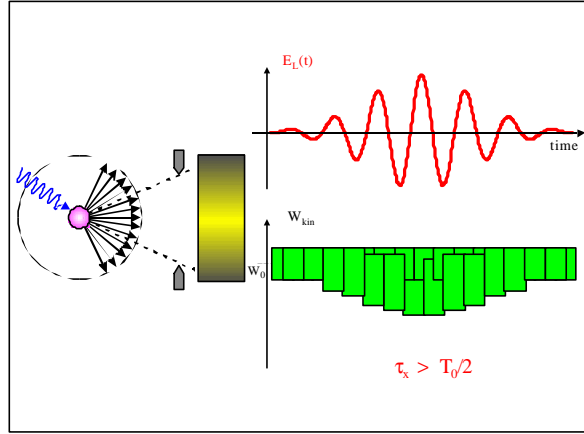


Figure 3.2: XUV pulse having a duration or a timing jitter exceeding $T_0=2$ ($\gg 1.25$ fs in our case) used for the cross-correlation smear out the modulation completely.

where $W_0 = \hbar \omega_x - W_b$; W_b is the initial kinetic energy of the photoelectron, ω_x denotes the XUV photon energy and W_b stands for the atomic binding energy of the electron liberated ($\hbar \omega_x - W_b$) and μ is the angle between the initial momentum of the electron and the laser electric field vector.

In order for the predicted variation of the photoelectron kinetic energy as a function of t_d to be compared with measurements, Eq. 3.5 needs to be generalized for a finite emission time slot of the photoelectron (corresponding to the finite XUV pulse duration) and for a distribution of initial kinetic energies over a finite energy range (reflecting the finite bandwidth of the XUV pulse). In addition, the distribution of initial kinetic energies as a function of μ has to be integrated over the finite detection cone to obtain a realistic prediction for the measured XUV photoelectron spectrum modified by the laser field.

For an XUV pulse short compared to half the laser period, i.e. $\omega_x \ll T_0=2$, and a fast (attosecond) response of the electronic transitions involved in the process, the predicted modulations in the initial kinetic energy distribution versus t_d survive these integrations and provide a sub-femtosecond probe for the measurement of the XUV pulse duration. A finite XUV pulse duration or a finite timing jitter of the XUV pulse (relative to the phase of the light field) of any origin results in a reduced depth of the resultant modulation of the width and center of gravity of the photoelectron energy spectrum (illustrated in Fig. 3.1). Figure 3.2 shows this fact in a very obvious way.

In fact, an XUV pulse duration or a timing jitter exceeding $T_0=2$ ($\gg 1.25$ fs in

our case) smears out the modulation completely [20]. The claim of a sub-femtosecond pulse duration relies on this line of argumentation: the modulation depth of $\text{CW}(t_d)$ provides a reliable upper limit, on an attosecond time scale, for XUV pulse duration and timing jitter.

3.1.2 Setup

Figure 3.5 displays the setup of our experiment. The XUV pulses exiting the neon harmonic source co-propagate with the laser pulses down the beam delivery tube. After 150 cm they hit a 200 nm thick zirconium foil with an aperture of 2 mm, which is the beam diameter of the harmonic beam due to the low divergence of ≈ 0.7 mrad. This filter is placed in the beam to block the laser and low-order harmonics, transmitting only photons with an energy of more than 70 eV. It is mounted on a nitrocellulose membrane of 5 μ m thickness and a hole in the middle, which - in the best case of production - has equal thickness over the whole area and does not introduce phase errors in the laser beam, which would wash out the temporal structure. This device, that is virtually dispersion-free at the laser wavelength, produces an annular laser beam with the XUV beam in the center. The energy in the laser beam is adjusted by a motorized iris and measured by a photodiode. Both the laser and the colinearly propagating XUV-beam are focused with a special multi-purpose mirror with a focal length of 35 mm. The mirror is mounted on a motorized stage so that it can be removed from the beamline. In this way the harmonic beam can be detected by a thinned, back-illuminated x-ray CCD camera for optimizing the radial intensity profile of the XUV beam (see Fig. 3.3). This can be done by fine adjustment of the position and pressure of the neon gas target and of the intensity of the laser pulses before HHG. Also mounted on a motorized wide-range translation stage, an XUV transmission grating can be inserted into the XUV beam.

The grating has 10^4 lines per mm or, in other words, a distance of $a = 100$ nm between the lines. This leads to an angle of $\mu_{\text{out}} = 7.5^\circ$ between 0^{th} and 1^{st} order, due to the grating equation

$$a(\sin \mu_{\text{in}} + \sin \mu_{\text{out}}) = m \lambda_x; \quad (3.6)$$

where $\mu_{\text{in}} = 0$ and μ_{out} are the angles of the in- and outgoing beams, m is the order of the interference maximum and λ_x is the XUV wavelength, in our case about 13 nm.

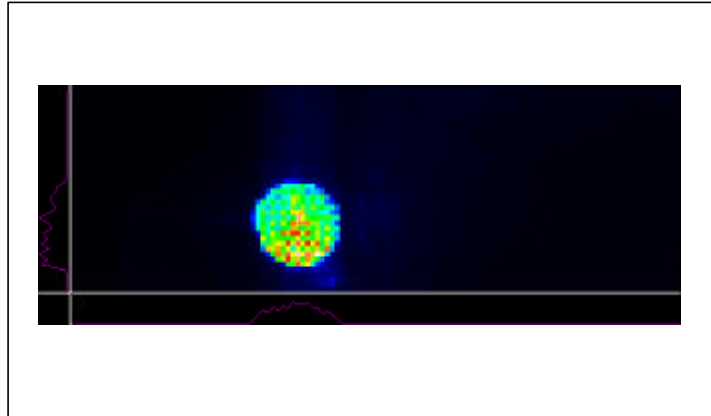


Figure 3.3: Online measured profile of the XUV beam used for adjustment optimization.

The CCD camera is angled to the measurement chamber over a flexible tube so that it can be moved either into the 0th or 1st order. In the 0th order the camera can be used for the aims described above. Moved in the 1st order it acts as a spectrograph able to resolve the XUV harmonics, due to a 30-cm distance from the grating and a CCD chip. In this way the XUV harmonic spectrum in the range of 10-15 nm can be monitored online (see Fig. 3.4). The spectra shown in Figure 2.7 have also been recorded with this apparatus.

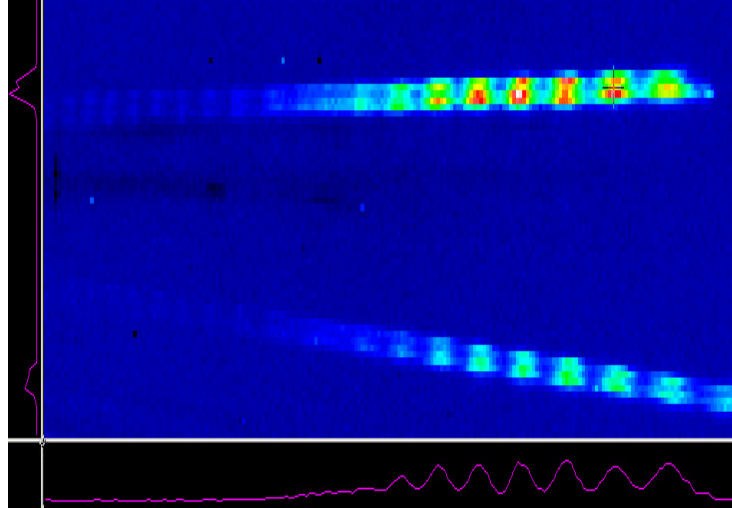


Figure 3.4: Online measured spectrum of XUV radiation. The oblique line is produced by the supporting mesh with line distances of 1 micrometer and can be used for calibration.

The XUV mirror is coated with a Mo/Si multilayer stack designed to reflect photons with 90 eV energy within a 5 eV bandwidth. This bandwidth is large enough to support XUV pulses as short as 0.4 fs. The mirror substrate consists of two concentric parts, matching the impinging laser and XUV beam. The outer part acts as a metallic mirror, reflecting the entire spectrum of the sub-10-fs laser pulses. The central piece is sitting on a piezo stage adjustable in transverse and longitudinal direction. In this manner the two pulses can be overlapped spatially and temporally in the focal plane, where a nozzle supplying the target atoms is situated. The wide-range piezo stage is able to introduce a delay of maximum $100 \text{ }^{\circ}\text{m}$ which corresponds to several tens of femtoseconds in time delay. Further, it offers a very precise in positioning (reproducibility of better than 10 nm), which allows to match the XUV pulse front to the light wave front within the volume of their interaction with nanometer-scale precision and stability, meaning a precision of better than 100 as in time delay.

The profile of the laser focus can be imaged by a lens on a CMOS camera for monitoring and course preadjustment of spatial overlap between the beams reflected by the two components of the Mo/Si mirror. The folding angle is kept below 5° to minimize astigmatism. The remaining spherical aberration gives rise to a time smearing of $< 0.05 \text{ fs}$ for the harmonic and of $\approx 1 \text{ fs}$ for the laser beam. The two focal spots of the XUV- and the laser beams have a diameter of approximately $2 \text{ }^{\circ}\text{m}$ respectively more than $20 \text{ }^{\circ}\text{m}$. In other words, the XUV beam spot size in the target was more than

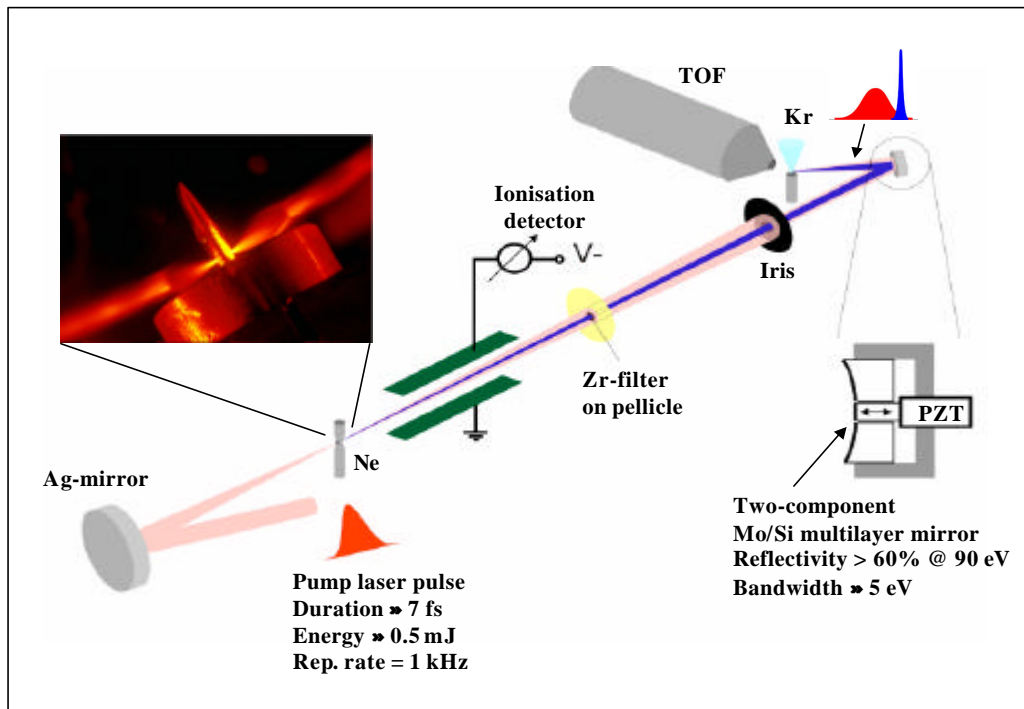


Figure 3.5: The schematic of the experiment. The focused 7-fs laser beam interacts with neon atoms to produce high-harmonic radiation. The laser and the highly-collimated XUV beam co-propagate collinearly through a 2-m beamline towards the measurement. In the beamline the laser and harmonic beams pass through a 200-nm-thick, 3-mm-diameter zirconium foil placed on a 5- μ m-thick nitrocellulose pellicle to cover a hole of 2-mm diameter. The energy transported by the resulting annular beam can be adjusted with a motorized iris between a fraction of a microjoule and a few tens of microjoules. The Mo/Si multilayer consists of an annular part having an outer diameter of 10 mm with a concentric hole of 3-mm diameter hosting a miniature mirror of slightly smaller diameter. Both parts originate from the same substrate, ensuring identical radii of curvature ($R = 70$ mm). The miniature central mirror is mounted on a wide range, nanometer precision piezo stage, allowing alignment and translation with respect to the external part.

an order of magnitude smaller than that of the laser beam, ensuring that all the XUV photoelectrons are exposed to the same light field, which is important for comparison with theory.

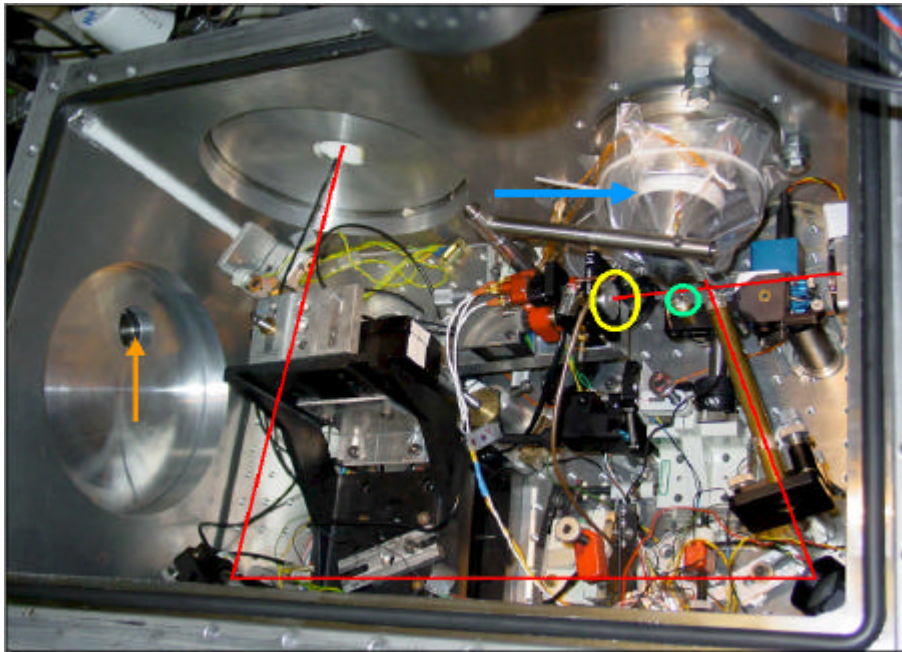


Figure 3.6: Experimental vacuum chamber. The red line shows the incoming laser - and XUV-beam and the way to the CMOS-camera, the yellow and the green circle mark the multilayer-mirror and the gas-nozzle, respectively. The blue arrow marks the TOF tube, the orange arrow points at the position of the CCD camera.

Krypton atoms emerging from the orifice of the nozzle, a metal-coated glass tube having an inner diameter of 50 μm , with a rate of 0.02 mbar l/s are photoionized by the XUV pulses in presence of the laser field. To avoid a constant photoelectron background due to ionization by the unfocused XUV beam, a thin shield is placed next to the krypton target. All parts in the vicinity of the spectrometer are conductively coated and properly grounded to avoid electrostatic charging.

The Kr 4p feature was chosen because of its nearly isotropic momentum distribution at $h\nu \approx 90$ eV photon energy (see Fig. 3.7) giving a favourable yield along the z-direction at our XUV photon energies. The photoelectrons originating from the 4s level (kinetic energy $\gg 62$ eV) are suppressed in this geometry due to their anisotropic momentum distribution [3]. The light pulse of peak intensity of $(1 \text{ to } 3) \times 10^{14} \text{ W/cm}^2$ overlapped with the more tightly focused XUV pulse in a volume of krypton gas kept at a pressure of a few times 10^{-2} mbar, limited to this value by space charge effects. The target chamber is evacuated by an 800 l/s turbo molecular pump to a pressure of about 10^{-6} mbar.

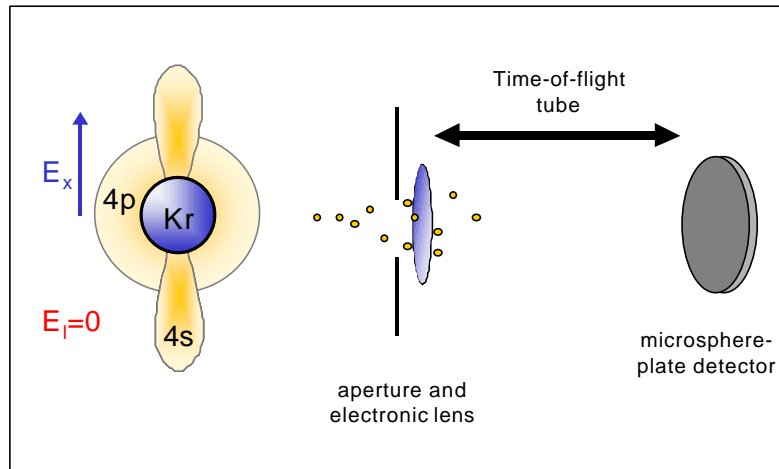


Figure 3.7: Principle of excitation and detection of Kr-electrons.

Appendix B contains the LabVIEW program, that allows on a calibrated attosecond timescale the control of the wide-range piezo stage and, therefore, the time delay positioning.

3.2 Detection and measurement

3.2.1 Time of flight spectrometer

Near the interaction area a time-of-flight spectrometer (TOF) is situated, counting the amount of emitted electrons due to the instant of detection, which can - as it is nothing else but a velocity distribution - be converted into energy-spectra. The photoelectrons from krypton atoms exposed simultaneously to a strong light field and an XUV pulse are detected within a cone aligned orthogonally to the electric field vector of the linearly-polarized light field. This orthogonal detection geometry was chosen to suppress a background in the photoelectron spectrum produced primarily along the electric field vector of the light pulse by above-threshold ionisation (ATI).

The entrance aperture of the time-of-flight TOF-photoelectron spectrometer (Fig. 3.8) having a diameter of 5 mm is placed at a distance of approximately 5 mm from the

interaction region, which corresponds to a solid angle of $\gg 0.3$ sr. Since the folding angle of the focusing mirror is kept as small as possible ($\gg 5^\pm$), the incoming beam passes the krypton source in close proximity.

The TOF spectrometer can be mechanically adjusted to optimize the acceptance angle and to center the electron source on the tube axis. The relatively large numerical aperture ($NA \gg 1$) of our TOF spectrometer is due to a carefully designed grid-free collecting electrostatic lens system optimized for the energy region of 50-100 eV, which has resulted in an order-of-magnitude improvement of detection efficiency as compared to conventional TOF tubes. Owing to the absence of meshes in the electron path distortion of the trajectories due to micro lensing by inhomogeneous electric fields close to the grid are avoided.

The electrostatic lens system consists of six concentric rings set to different electric potentials ($U_{1,6}$) bending the electron trajectories towards the axis. The adjacent drift tube is magnetically shielded to avoid deflection of the electrons due to stray magnetic fields. Application of a retarding voltage of -20 V to the 40 cm long 5-metal shielded drift tube improves the energy resolution by lowering the electron velocity. The spectrometer can be operated to provide almost flat transmission for kinetic energies ranging from 40 eV to 80 eV. However, in order to optimize the sensitivity for the Kr-4p photoline the lens voltages were chosen to obtain maximum transmission at $\gg 75$ eV with a cut-off above 100 eV. Under these conditions the spectral resolution is still better than 1 eV.

Particular attention has been paid to a careful choice of the electronic acquisition system for the transient signal from the electron detector at the rear of the TOF drift tube. If directly acquired with a digital oscilloscope, the resulting waveform actually represents a convolution of the electron spectrum with the temporal response of the microsphere plate (MSP) detector to a single electron event in the time domain. Even if the detector anode is carefully designed to avoid pulse distortion and ringing the achievable temporal resolution with this technique will not exceed 1-2 ns. If needed, substantially improved resolution (down to some 200 ps) is possible with time-resolved single event counting by evaluating the rising edge of the detector pulse in a constant-fraction discriminator followed by a time-to-amplitude converter, an analog-to-digital converter and a multichannel analyzer.

During data acquisition each laser pulse generates the start trigger for a time-to-

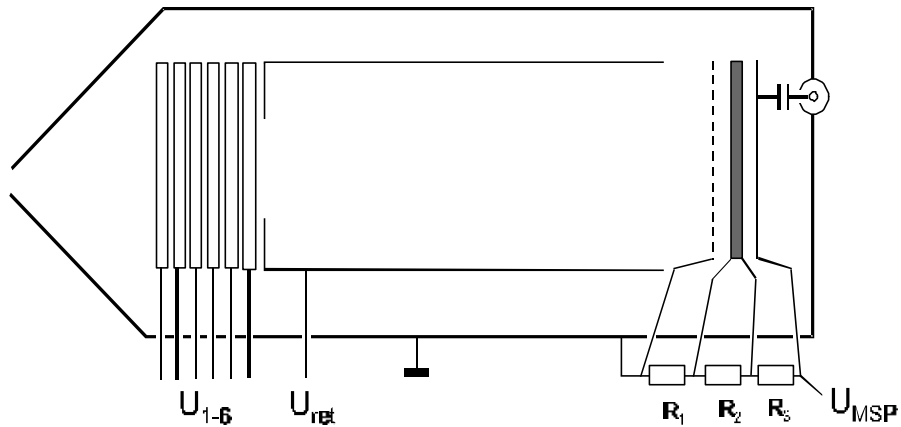


Figure 3.8: Schematic of the time-of-flight electron spectrometer. Overall length is 40 cm, tube diameter is 6 cm. $R_1 = R_3 = 3.3 \text{ M}\Omega$, $R_2 = 22 \text{ }\Omega$

amplitude converter (TAC) via a photodiode. The stop pulse is derived from the MSP detector signal. The output of the TAC is read out by a computer and accumulated in a multi-channel pulse height analyser. The resulting time spectrum has a resolution of $\Delta t = 0.464 \text{ ns/channel}$ with 1024 channels in total. Figure 3.9 shows two time spectra showing different distributions as far as the width of the peak is concerned.

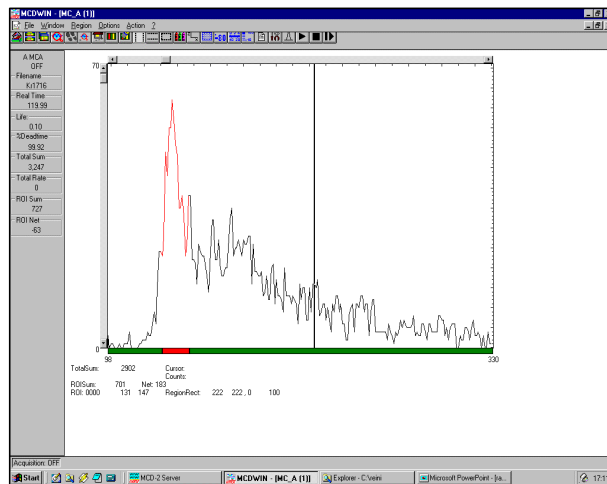
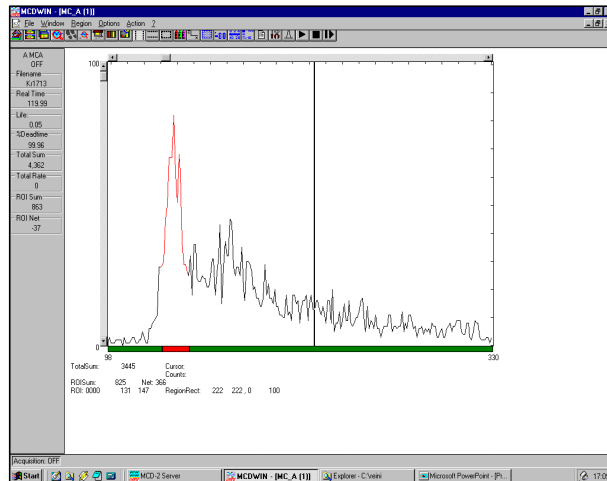


Figure 3.9: Two different Time-of-flight spectra, showing the amount of photoelectrons detected over the time delay after emission. The x-axis starts with the shortest flight-time meaning highest energy. The noise at the low energy tail are ATI electrons. As they are pronounced by the detection system, they are downscaled at the evaluation of the measurement data.

The time scale is converted to energy according to

$$E = \frac{L_{e^{\otimes}}^{\#2}}{((i + i_0)\zeta_i \zeta_0)} + U_{e^{\otimes}}; \quad (3.7)$$

with i being the channel number and i_0 depending on the length of the start trigger line and the internal delay of the TAC. $L_{e^{\otimes}} = 501:01 \text{ ns} \otimes V^{1=2}$ is the length of the flight tube weighted with the square root of the effective electron mass, $\zeta_0 = 12:01 \text{ ns}$ a correction of the flight time and $U_{e^{\otimes}} = \text{; } 19:36 \text{ eV}$ the effective potential caused by the retardation voltage $U_{\text{ret}} = \text{; } 20 \text{ V}$. Alternatively the flight time spectra can be recorded

with a fast oscilloscope (TDS 520 D, Tektronix).

3.2.2 Measuring procedure and acquisition of measurement data

Before the XUV/laser-field cross-correlation can be recorded by measuring the XUV photoelectron spectrum as a function of t_d the temporal overlap between the two pulses has to be found. To this end, we generate ATI electrons upon removing the Zr-filter (stopping the central fraction of the laser beam, see Fig 3.5) from the beamline and by focusing both the inner and the annular part of the laser beam with the two-component Mo/Si-multilayer mirror onto the krypton target. Scanning the delay between outer and inner part of the mirror with a feedback-controlled piezo translator, an 'interferometric' ATI auto-correlation of the 7-fs laser pulse can be recorded. Fig. 3.10 shows the detected electron count rate as a function of the delay between the two replicas of the laser pulse.

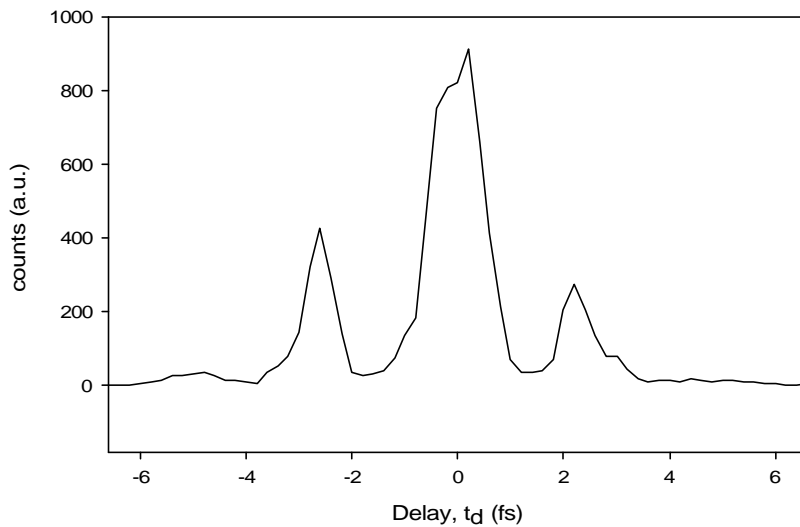


Figure 3.10: ATI-electron auto-correlation

Owing to the strongly nonlinear dependence of the ionization rate on the electric field strength and the few-femtosecond pulse duration, the trace is confined to virtually a single laser cycle. The central peak indicates the delay of optimum temporal overlap between the two beams. From this reference, the zero delay between the XUV and

laser pulse can be inferred by taking into account the finite ($\gg 5 \mu\text{m}$) thickness of the pellicle holding the Zr-foil, which is reintroduced for the XUV/laser-field cross-correlation measurements. More recently, owing to an increased photoelectron flux we were able to measure the shift of the high energy spectral tail of the XUV photoelectron spectrum following the spectral broadening as a function of time delay between laser and XUV pulses. This was used as an indicator of time delay, so it was possible to find the temporal overlap of the two beams' intensity maxima without removing the filter mounted on the pellicle. Appendix C shows the LabVIEW program controlling this feature.

To record the cross-correlation depicted in Section 3.1.1, the delay t_d is varied in steps of $\Delta t_d = 150$ as in the central range of temporal overlap ($-5 \text{ fs} \leq t_d \leq 5 \text{ fs}$, with $t_d = 0$ approximately at the peak of the light pulse) and of increased step size outside this range.

Figure 3.11 shows two representative Kr-4p spectra corrected for (a constant) ATI background and recorded at $t_d = \pm 450$ as and $t_d = 0$ as, along with respective asymmetric Gaussian fits. This model function yields excellent fits to our data, characterized by a fidelity parameter $R^2 > 0.95$. It has to be emphasized, that the significant broadening and shift of the center of gravity between these two spectra takes place within only 450 as. The enhanced noise at lower energies can be attributed to ATI electrons.

The contour plot in Figure 3.12 comprises some 120 spectra of the 4p feature (processed as described above) as a function of delay t_d . Each spectrum was normalized to the same number of counts, resulting in a constant area under the spectral distribution functions. Owing to the relatively large solid angle of detection, providing a high number of electron counts, the overall measurement time could be limited to $\gg 5$ hours. The data clearly bring to light a quasi-periodic evolution of the photoelectron energy spectrum with a period of $\gg T_0=2$. The most pronounced modulation versus t_d appears at the peak of the spectra. With the total number of electrons per spectrum fixed, this is a direct consequence of the modulation of spectral width, mentioned in Section 3.3.2.

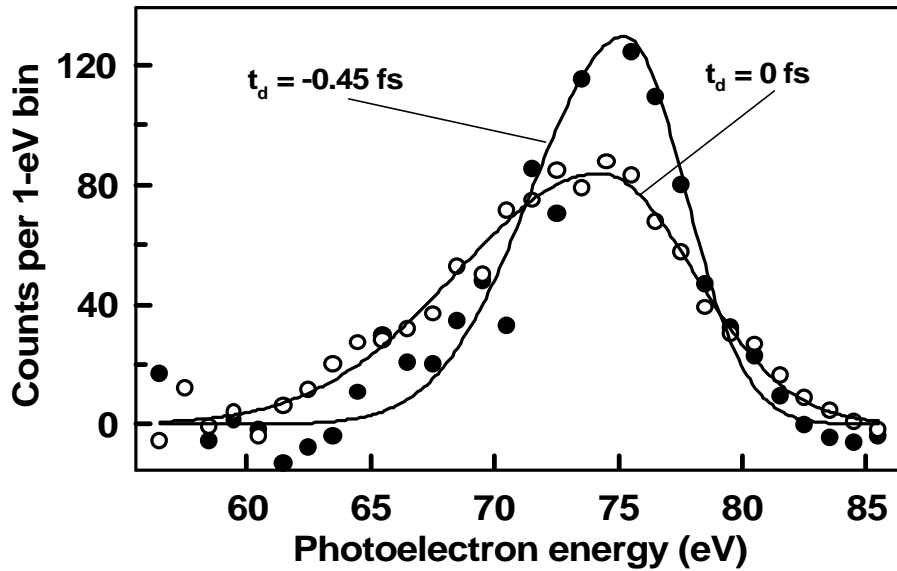


Figure 3.11: Kr-4p photoelectron spectra produced by ≈ 90 -eV XUV pulses in the presence of a strong visible light field at two different delays of the XUV pulse with respect of the light wave. The dots represent spectra corrected for some ATI background from the measurements performed by a time-of-flight electron spectrometer. The lines show asymmetric Gaussian fits to the data.

Compared to theoretical predictions (see Fig. 3.1) the result of the measurement scan shown in Figure 3.12 is in excellent accordance.

The measurement procedure has been automated in the latest time by a LabVIEW code, which can be found in Appendix D.

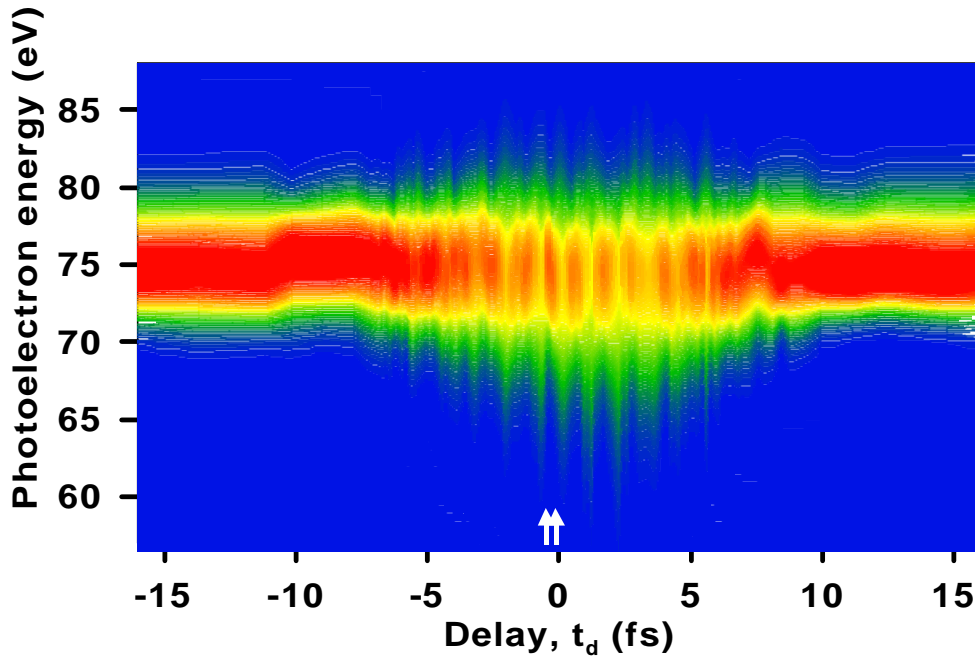


Figure 3.12: Energy distributions of the Kr-4p photoelectrons as a function of the delay t_d between the light wave and the XUV pulse over some tens of femtoseconds (evaluated from asymmetric Gaussian τ 's). The 2 white arrows point at the positions of the two spectra shown in Figure 3.11

3.3 Interpretation of the results

3.3.1 Ab initio calculations: duration of isolated pulses

In order to evaluate the XUV pulse duration from our XUV/visible light-field cross-correlation data (insert in Fig. 3.13) we introduce a measure for the depth of modulation of $\mathcal{C}W(t_d)$, the fringe visibility

$$FV = (\mathcal{C}W_{\max} - \mathcal{C}W_{\min}) / (\mathcal{C}W_{\max} + \mathcal{C}W_{\min} - 2\mathcal{C}W_1); \quad (3.8)$$

where $\mathcal{C}W_{\max}$ and $\mathcal{C}W_{\min}$ stand for adjacent local extremal values of $\mathcal{C}W(t_d)$ as a function of the delay time and $\mathcal{C}W_1 = \mathcal{C}W(t_d - 1)$, and measured the local fringe spacing (FS). The central portion of the correlation function $\mathcal{C}W(t_d)$, with maximum FV and minimum FS, provides optimum resolution for determining the XUV pulse duration. A sinusoidal fit to the two central modulation periods (see red line in Fig.

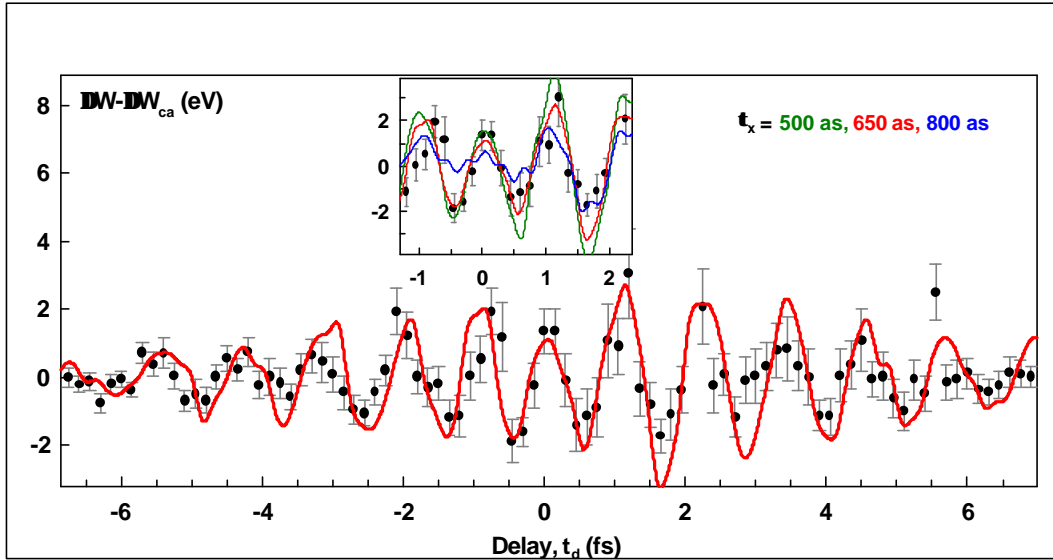


Figure 3.13: Oscillating component of the spectral width, $\Delta W - \Delta W_{ca}$ (eV) of the Kr-4p photoelectron spectra as a function of the delay t_d between the light wave and the XUV pulse, where $\Delta W_{ca}(t_d)$ stands for the cycle-averaged value of $\Delta W(t_d)$. The dots are the measured results. The full line is the result from simulations based on the quasi-classical theory of two-colour XUV photoionisation by assuming a frequency-swept (see Section 3.3.2), 7-fs, 780-nm linearly polarized light field of 5×10^{13} W/cm² peak intensity and a 650-as, 90-eV Gaussian XUV pulse. The insert shows these simulations for different XUV pulse durations t_x .

3.13) yields $FS = 960$ as $\S 30$ as (corresponding to half an oscillation-cycle of the fundamental light, see below) and $FV = 0.30 \S 0.03$.

For comparison with the measured data (dots in Fig. 3.13), we simulated the light-field-induced variation of the Kr-4p photoelectron spectrum versus t_d based on the quasi-classical model described above. The duration t_x of our Gaussian model XUV pulse was used as the only fit parameter. The visible light pulse was also modelled with a Gaussian intensity envelope peaking at 10^{14} W/cm², carrying a quadratic frequency sweep to account for the frequency upshift present at the center of the measured correlation function $\Delta W(t_d)$. Best agreement between measured (dots) and calculated data (red line in Fig. 3.13) was achieved for XUV pulse durations in the range of 600 as $\cdot t_x \cdot 700$ as, yielding a fringe visibility of $FV = 0.30 \S 0.05$ in the correlation

function near $t_d = 0$ as. Assuming pulse durations of $\tau_x = 500$ as and $\tau_x = 800$ as, respectively, the FV is enhanced and suppressed with respect to the measured value well beyond the experimental error of 10%. Therefore, $\tau_x = 650$ as ± 150 as represents a safe estimate for the duration of our 90-eV XUV pulse. The sensitivity of the method is underlined by the computed FV decreasing by a factor as large as three (from 0.30 to 0.10) as the XUV pulse duration is increased from 650 as to 900 as, with the modulation in $\phi W(t_d)$ disappearing for $\tau_x \gg 1$ fs.

3.3.2 Single pulses

If it comes to using sub-femtosecond pulses for spectroscopic applications, it is an essential question whether this sub-femtosecond pulse is accompanied by one or more satellite pulses spaced by $\gg T_0=2$ as observed in a recent experiment [16]. A concomitant of the emergence of equidistant satellite pulses is the appearance of spectral sidebands (at twice the photon energy of the driver laser) of rapidly increasing magnitude with increasing weight of the satellite pulse(s). The absence of any significant modulation in our XUV harmonic spectrum reflected by the Mo/Si multilayer limits the possible satellite fluence to less than 10% of the total XUV fluence.

Fig. 3.14 shows the measured photoelectron spectra, full and dashed lines, reflected those of the generating XUV pulses produced laser pulses of 7 fs and, for comparison, 12 fs in duration, respectively. The latter spectrum indicates that the weak modulation of the 7-fs-pulse-produced XUV spectrum is not due to finite spectral resolution of the TOF detector or some smearing effects due to propagation of the pump laser pulse through an extended generation medium. Further confirmation of the low weight of XUV satellite pulses is supplied by results summarized below.

The agreement of the measured XUV pulse duration and that obtained from our numerical calculations [67] within the experimental error suggests that the timing jitter of the XUV pulse with respect to the phase of the visible light wave must be small compared to 1 fs. As a consequence, our experiment bears evidence of the sub-femtosecond XUV pulse being locked to the carrier wave of its generating few-cycle light pulse with attosecond precision. This indicates a surprising robustness of the high-order harmonic generation process against random shifts of the absolute phase [6], i.e. of the position of the carrier with respect to the amplitude envelope. The attosecond timing stability of our sub-femtosecond XUV pulse to a few-cycle visible light wave makes these pulses

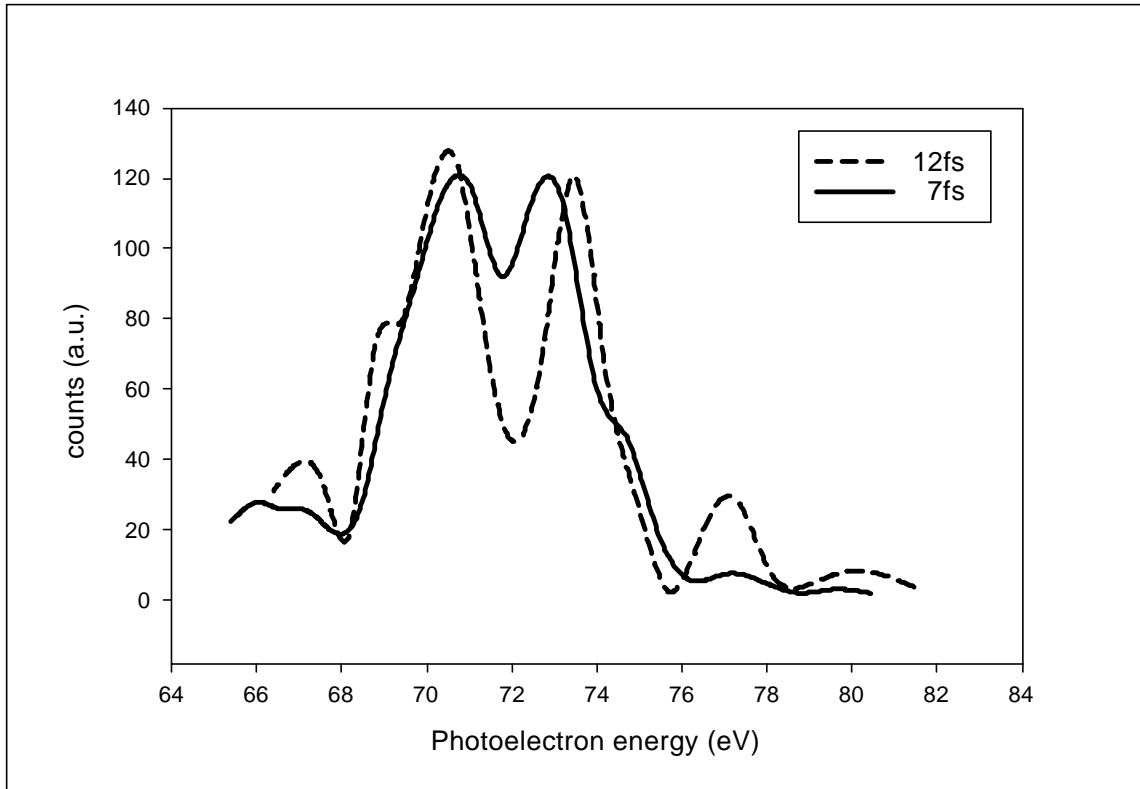


Figure 3.14: Photoelectron spectra of XUV pulses generated by 7 fs respectively 12 fs laser pulses.

a unique tool for investigating the dynamic behaviour of matter on an attosecond time scale. Our light-field-controlled photoemission experiment already demonstrates this capability. In the measured energy distribution $\mathcal{C}W(t_d)$ it is implicit, that in the investigated spectral range near 90 eV bound-free electronic transitions from the 4p state in krypton respond to XUV excitation within less than 500 as. This is what we believe the first truly attosecond measurement.

With its duration extracted from the central part of $\mathcal{C}W(t_d)$ in Fig. 3.13, the XUV pulse may now also be used to probe the evolution of the electric field in the few-cycle light pulse. The sweep of instantaneous frequency ω_{inst} (or wavelength λ_{inst}) in the visible light pulse can be evaluated from the modulation in $\mathcal{C}W(t_d)$ by fitting a sinusoidal half-oscillation of adjustable period to the data in Figure 3.13. The sampling interval was scanned through the range of $-8 \text{ fs} \leq t_d \leq 8 \text{ fs}$. The dots in Fig. 3.15 show the carrier frequency sweep evaluated in this manner, revealing a dynamic blue shift from a carrier wavelength of $\approx 780 \text{ nm}$ to $\approx 550 \text{ nm}$. To understand this finding

we have to remember that the light pulse used here is derived from the one generating the high harmonics.

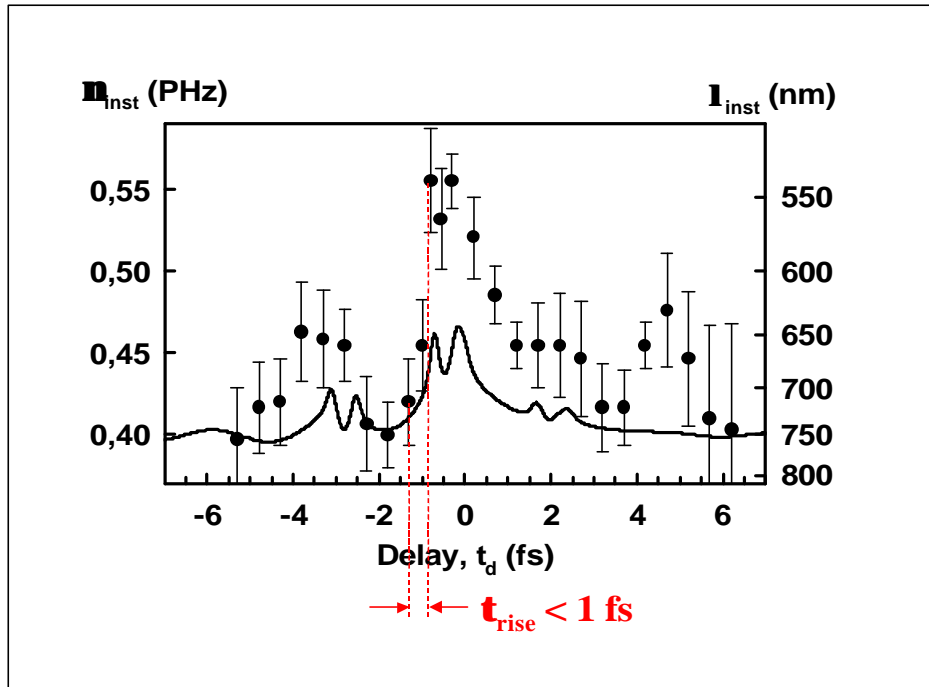


Figure 3.15: Calculated (line) and measured blueshift of the fundamental pulse, probed by the XUV pulse. The steep rising edge indicates the presence of single XUV pulses without significant satellites.

The line in Fig. 3.15 is obtained from propagating a bandwidth-limited 7-fs laser pulse through the volume of neon gas emitting the high harmonics in a numerical experiment [57] and exhibits a dynamic frequency shift at the pulse center originating from self-phase modulation due to ionization of the neon gas in the harmonic source. The measured $\gg 30\%$ dynamic frequency blue shift at the center of the pulse is larger than predicted by our numerical study but reflects qualitatively the predicted behaviour.

This qualitative agreement suggests that the observed blue shift can be attributed to ionization-induced self-phase modulation in the high harmonic generation process. The presence of this substantial frequency sweep in the light pulse employed for controlling XUV photoemission provides a further strong argument for the isolated nature of our XUV pulse: any satellite pulse of notable energy would significantly suppress fringe vis-

ibility near $t_d = 0$, where the modulation period of the cross-correlation trace $\mathcal{C}W(t_d)$ is substantially shorter than the predicted temporal spacing of possible satellites. The achieved direct probing of the electric field oscillations in a light wave as implemented here is another demonstration of attosecond metrology. It will permit complete measurement of the electric field of absolute-phase-stabilized few-cycle light [29, 68].

Regarding these promising results of single, isolated sub-femtosecond pulses accompanied by few-cycle high intensity laser pulses in the visible range at a high repetition rate, it can be concluded, that the main tools for attosecond spectroscopy are now available. This will be addressed in the following chapter.

3.4 Expedited attosecond diagnosis

Another straightforward method of measuring the duration of sub-femtosecond pulses is shown in Figure 3.16. Using a geometry, where both the laser and the XUV electric field are parallel to the direction of detection of the photoelectrons, the spectra experience no broadening but only a shift in energy. This is a major difference compared to the geometry described in Section 3.1.1, where the electric laser field was applied orthogonally to the direction of detection causes a broadening of the spectra, as well.

The essential point now is, that this shift without substantial broadening only happens if the generated XUV burst (and therefore the generated photoelectron wavepacket) is very short compared to the laser field half oscillation period $T_0=2$ (see Figure 3.16). If the XUV pulse and therefore the electron wave packets exceeds $T_0=2$, different portions of the wavepacket experience different momentum transfer and the original XUV spectrum is subjected a multiple shift by $E = \hbar\omega_L$ (see Figure 3.17). This results in a large spread of energies.

The false-colour contour plot of the photoelectron spectra in Figure 3.18 shows very impressingly the calculated effect on the electron spectra depending on the ratio of XUV pulse duration τ_x to the fundamental laser oscillation cycle T_0 . Down to a relation of $\tau_x = T_0=5$ the multiple shift by $E = \hbar\omega_L$ can be seen beautifully. For $\tau_x < T_0=5$ and for the electron wave packet centered to the zero-transition of the laser electric field a considerable shift is achieved, resulting in the minimum and maximum final electron energy of

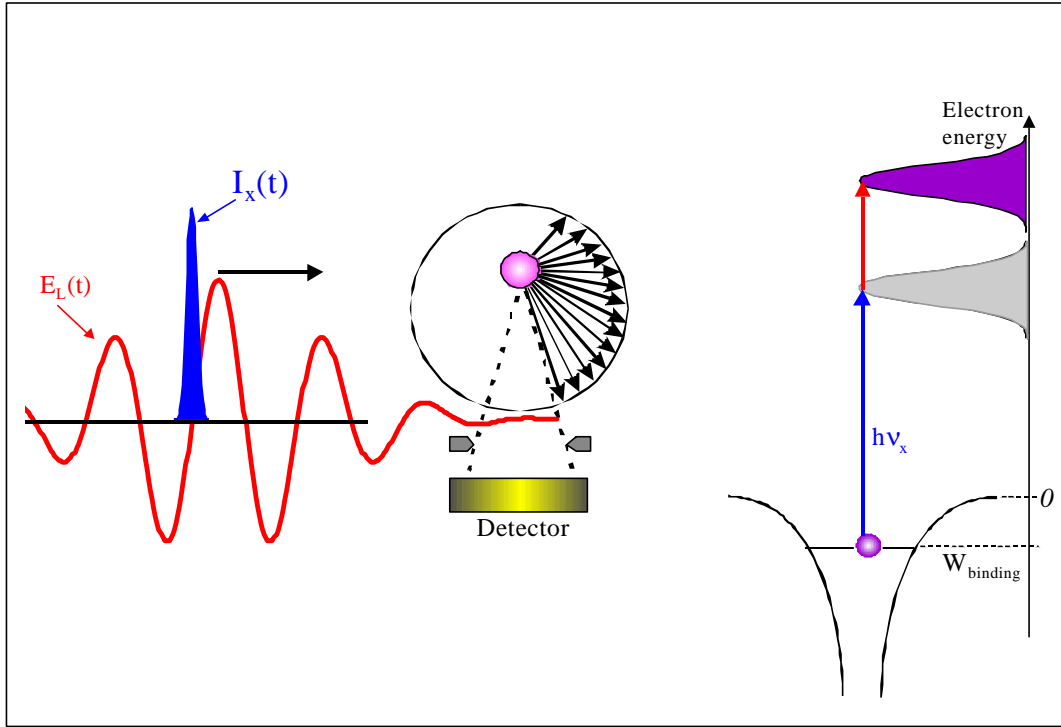


Figure 3.16: XUV photoelectrons generated by a few-cycle pulse moving along the laser polarization

$$W_f = W_0 + 2U_p(t_d) \mathcal{S} \mathcal{C}W; \quad (3.9)$$

with

$$\mathcal{C}W = [8W_0U_p(t_d)]^{1=2}; \quad (3.10)$$

where U_p is the ponderomotive potential, the electron's quiver energy averaged over an optical cycle (see Eq. 3.4).

Figure 3.19 and 3.20 display electron energy spectra as a function of the measured relative change of E_L in a false-colour representation. In the absence of a light field, the photoelectron energy spectrum (lowest plot on the right of Figure 3.20) mimics that of the XUV pulse downshifted by the ionization potential of neon ($W_b = 21.5$ eV). Figure 3.19 summarizes data obtained when the peak intensity of the harmonic driver was adjusted to 650-700 TW/cm² to produce discrete harmonic spectra within the range of 85-100 eV. The quasi-periodic time structure of the emission with a period length evaluated as $\gg 1.25$ fs from the violet spectrum in Figure 2.7 suggests that the

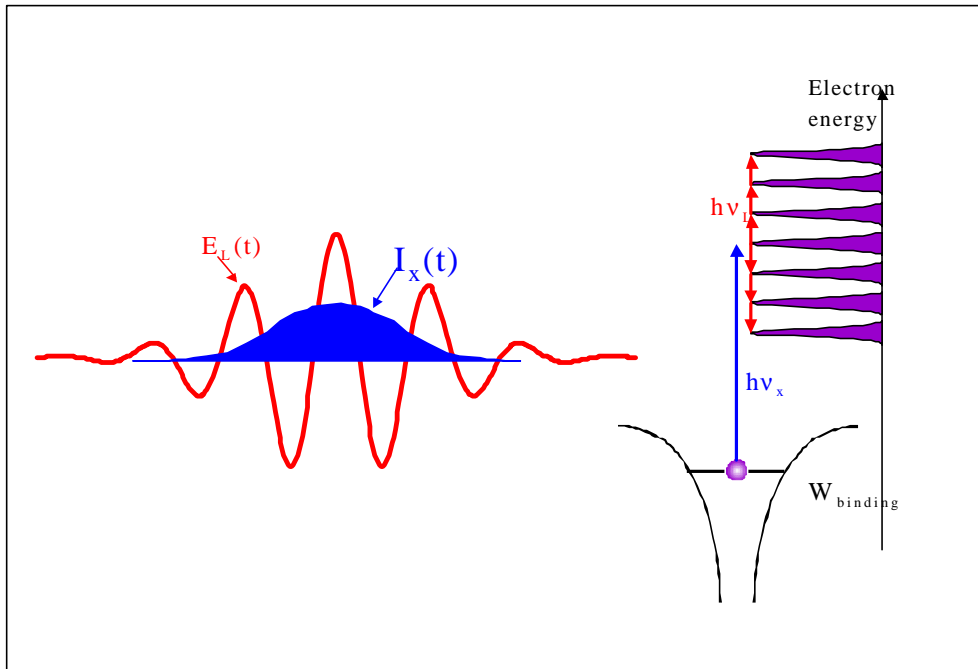


Figure 3.17: XUV photoelectrons generated by a multi-cycle pulse moving along the laser polarization

timing of each spike in the emerging pulse sequence might fulfill

$$\Delta t_d + \tau = \frac{1}{2}T_0 + m\frac{1}{4}T_0 \quad (3.11)$$

Hence only an up- and downshifted spectral feature would be expected, if the spikes weren't longer than $T_0=5$. A blue-shift near the laser pulse peak (induced by ionization in the harmonic generation process, see Section 3.3.2) tends to impair synchronism between the XUV pulse sequence and the zero transitions of the probe laser field. However, it can not fully account for the dramatic energy spread occurring for the highest applied fields in Figure 3.19. The observed energy spread can only be reconciled with the spikes carrying a substantial chirp and hence being broadened significantly beyond $T_0=5$. Intuition and simulations support the presence of enhanced phase distortions in the 'plateau' region of the harmonic spectrum.

The data depicted in Figure 3.20 have been collected with the intensity of the harmonic driver adjusted in the range of 400-450 TW/cm² to generate a continuous harmonic spectrum near 100 eV. In a striking contrast with the behavior shown in

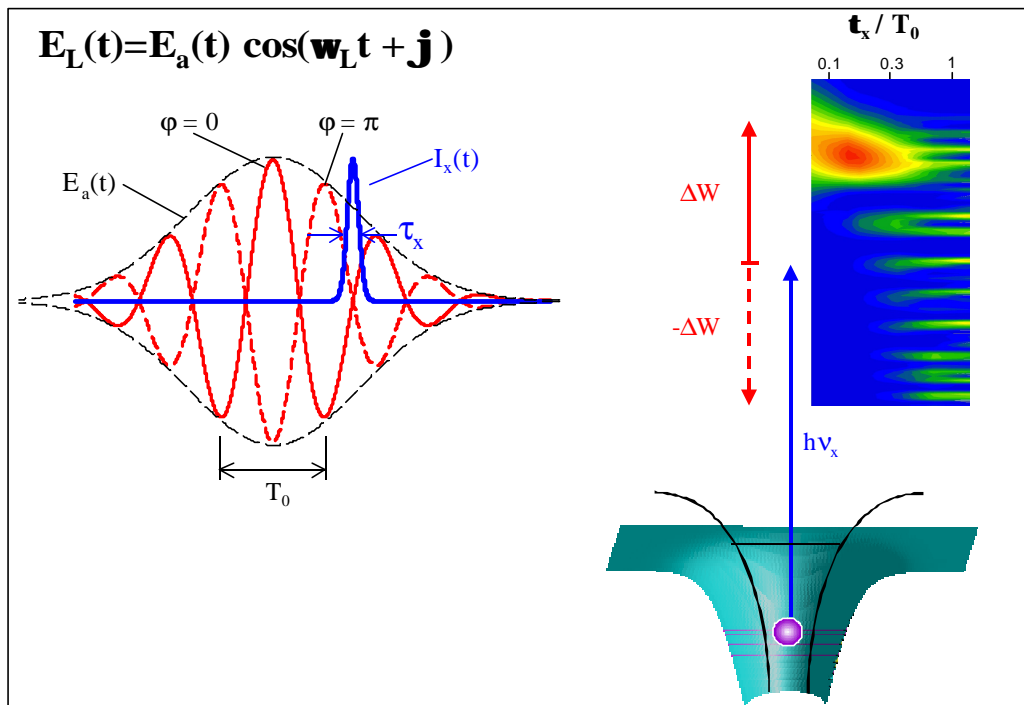


Figure 3.18: Effect on the electron spectra depending on the relation between XUV pulse duration τ_x and the fundamental laser oscillation cycle T_0 .

Figure 3.19, with increasing field strength the electron energy spectrum is upshifted as a whole without a dramatic distortion of its shape. The simultaneous appearance of an up- and down-shifted spectral feature is the consequence of pump pulses with $\phi = 0$ and $\phi = \pi$ contributing to the electron spectra accumulated over many laser shots, i.e. of the lack of phase stabilization of our sub-10-fs laser pulses. The downshifted feature gets increasingly washed out for increasing E_L due to modifications in the angular momentum distribution by the decelerating momentum transfer within the finite detection cone.

This series of upshifted photoelectron spectra indicates that the electron wavepacket must be temporally confined to a small fraction of $T_0=2$ and released when $E_L(t_d) \approx 0$, in accordance with the results of numerical simulations [61]. The dotted regression line in Figure 3.20 displays a linear dependence of the energy shift on the light field strength and corroborates the classical prediction (Equations 3.9 and 3.10). As a matter of fact, the measured spectra can be well reproduced by simulating the electron wavepacket as a classical ensemble of electrons having a distribution of initial energies and release times,

whose motions are governed by the laws of classical mechanics and electrodynamics. Approximating the initial energy distribution with a Gaussian function (bottom red line in Figure 3.20) and assuming a bandwidth-limited XUV pulse ($\zeta_x \approx 200$ as) that peaks at $E_L(t_d) = 0$, the classical (just as the quantum) analysis delivers results (central and upper full red lines in Figure 3.20) in good agreement with the spectra measured for different strengths of $E_a(t_d)$. Attosecond confinement appears to mask quantum effects in the interaction of photoelectrons with strong light.

The generation of isolated sub-femtosecond XUV pulses synchronized to a strong few-cycle light pulse [61] opened up a route to time-resolved (pump-probe) inner-shell atomic spectroscopy by employing the XUV pulse as a pump and the light pulse as a probe [69]. Indispensable to the routine application of this new tool is a reliable, simple, and fast diagnostics of its key characteristics. These include the strength and phase-stability of the few-cycle probe field, the timing jitter between the XUV pulse and light wave and the duration of the XUV pulse. The sensitivity of the energy spectrum of the XUV-induced, light-accelerated photoelectrons to these parameters makes it an ideal diagnostic tool for attosecond spectroscopy.

Owing to the favourable timing of the subfemtosecond harmonic pulse to its few-cycle driver, $E_L(t_d) \approx 0$, the photoelectron energy shift in Figure 3.20 directly probes the instantaneous electric field amplitude $E_a(t_d)$ with an accuracy of better than 10%, providing direct experimental access to the peak electric field strength of an intense light pulse. Moreover, the light-steered electron proves a sensitive probe of the absolute-phase stability of intense few-cycle light. For ϕ being firmly locked to zero the photoelectrons would be exclusively accelerated (with the convention of $E_L > 0$ implying a field vector that points towards the electron detector). This would imply a disappearance of the downshifted spectral feature, offering a reliable diagnostics of the phase stability of intense few-cycle pulses for future phase-stabilized systems.

Timing jitter between the XUV pulse and the probe light phase affects the temporal resolution to the same extent as ζ_x and T_0 [69], hence its measurement is imperative for attosecond spectroscopy. The periodic harmonic structure can be perceived in several downshifted spectra, e.g. central plot in Figure 3.20 (the structure tends to get blurred in the upshifted features because of time-of-flight resolution worsening for increasing electron energy). An analysis of these spectra results in the conclusion that smearing of the electron spectrum accumulated over many laser shots due to fluctuations in $E_L(t_d)$

(by either laser intensity variations or XUV pulse timing jitter) is less than $\lesssim 10\%$ of the energy shift ΔW . From simulations of the electron energy spectrum for slightly different values of t_d we inferred a shot-to-shot timing stability of the XUV pulse to the phase of its few-cycle driver of better than $\lesssim 200$ attoseconds.

Figure 3.19 and 3.20 confirm that the energy spectrum of the light-accelerated XUV photoelectron responds sensitively to temporal broadening of the ionizing XUV pulse. Although a conspicuous energy spread is predicted to come into play only as t_x becomes longer than $T_0=3$, a considerable narrowing of the energy-shifted spectral feature already sets in for $t_x > T_0=10$, accompanied by the appearance of a prominent downshifted satellite for $t_x > T_0=5$. Figure 3.20 shows the energy distributions calculated under the assumption of the measured XUV spectrum carrying a quadratic spectral phase adjusted to yield $t_x = T_0=5 = 500$ as (dashed lines). By the same token, simulations with higher-order phase distortions adjusted to broaden the XUV pulse to $\gg T_0=5$ gave rise to significant discrepancies for the entire series of spectra recorded at different field strengths. The deviations can not be accounted for by spectral smearing effects that are limited to $\Delta W=10$ as concluded above. Contrasting these discrepancies with the good agreement of the series of upshifted spectra measured and computed under the assumption of a bandwidth-limited XUV pulse (two of which are depicted with full red lines in Figure 3.20) $t_x < T_0=5$, implies a safe upper limit of $t_x < T_0=5 = 500$ as on the XUV pulse duration.

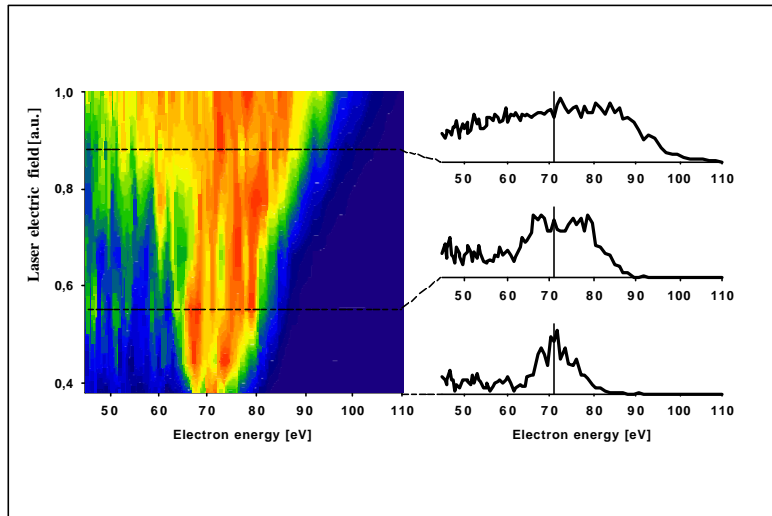


Figure 3.19: Photoelectron spectra generated by soft-XUV pulses having a discrete harmonic spectrum in the 85-100-eV spectral range. For increasing field strength the relative spectral intensity for $W < W_0 \approx 71$ eV decreases and spreads due to an increasing number of electrons detected out of the detection cone due to a decelerating momentum transfer.

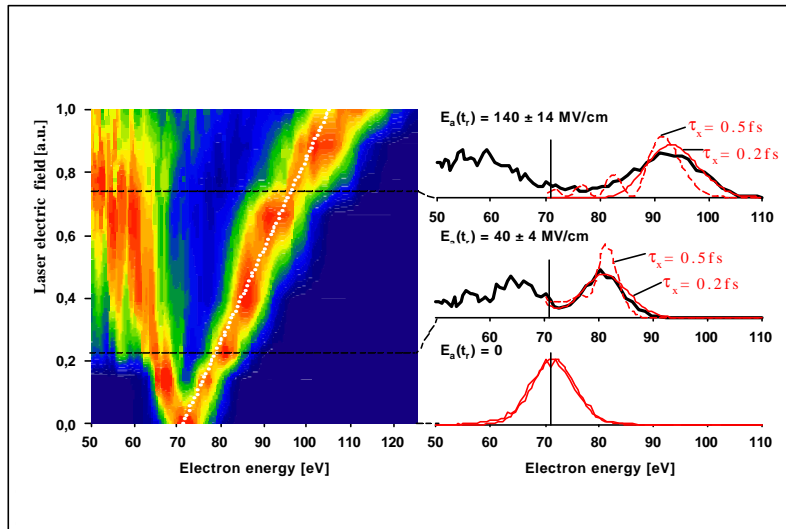


Figure 3.20: Photoelectron spectra generated by XUV pulses having a continuous harmonic spectrum in the 85-100-eV spectral range. $E_L(t_d)$ has been evaluated from the observed energy shift. The bottom red line is the model XUV spectrum (downshifted by the electron binding energy of 21.5 eV) used in the simulations resulting in the central and upper red lines for bandwidth-limited 200-as (full lines) and chirped 500-as soft-XUV pulses (dashed lines).

Chapter 4

Time-resolved attosecond spectroscopy

This chapter shall give an overview about concepts and current experiments that show how pump/probe spectroscopy of molecular and atomic excitation and relaxation processes - such as e.g. optical-field ionization and inner-shell relaxation processes - can be traced directly in the time domain by drawing on low-energy isolated XUV pulses in combination with synchronized strong few-cycle laser pulses, i.e. tools that are available now.

4.1 Basic tools

Pump/probe experiments turned out to be the most direct approach to time-domain investigations. The limitation until now to go into smaller and shorter regimes, e.g. where motions of bound electrons in excited atoms take place, was set by the required combination of short wavelengths (i.e. high photon energy) and sub-femtosecond pulse duration, constituting challenging demands. The generation of sub-femtosecond XUV pulses was not the only hurdle. Unfortunately, the generation of attosecond pulses is mostly stuck to the production of a pulse train, which was pointed out in Section 2.2.4. This fact acts as a major problem for time-resolution: Since the very short ($\gg 1$; 2 fs) pulse intervals within the train prevents an unambiguous interpretation of sampling, straightforward interpretation of spectroscopic data requires isolated, single pulses [17, 18]. Using few-cycle pulses as a driver for HHG, the demand of single, iso-

lated pulses could be satisfied, so it is now possible to extend time-resolved spectroscopy into the attosecond domain. Figure 4.1 shows the outline of a XUV-pump/XUV-probe experiment, where these pulses are used for both triggering and probing bound-bound or bound-free transitions in atoms or molecules. For tracing atomic inner-shell relaxation processes either photoelectron- or Auger-spectra can be used.

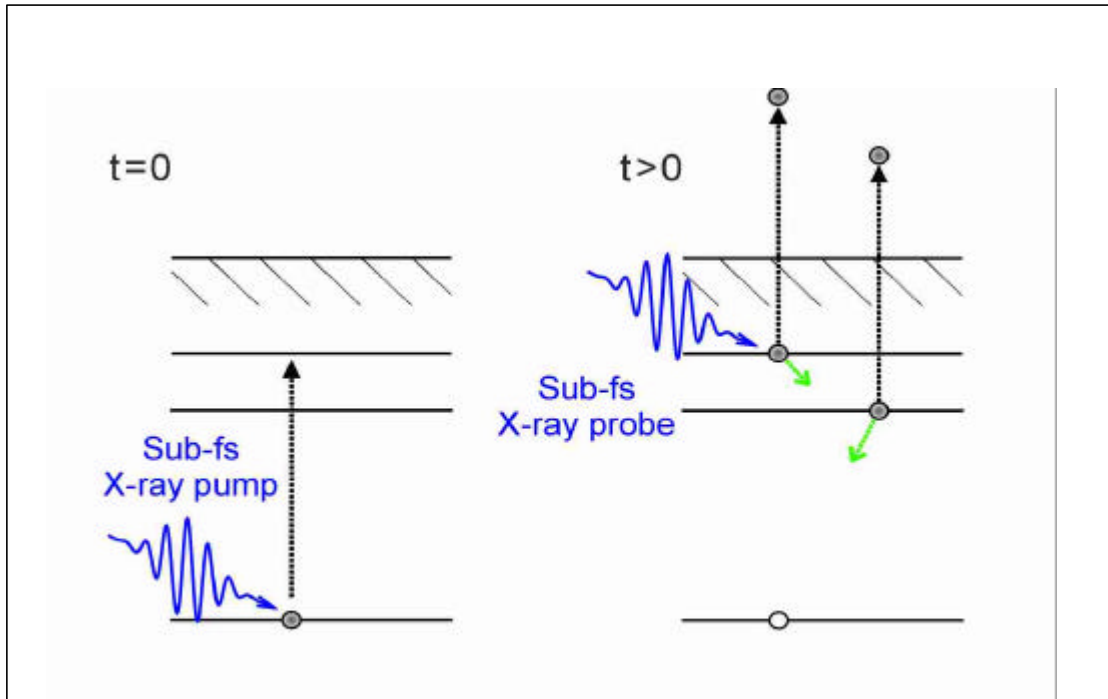


Figure 4.1: Tracing inner-shell relaxation processes by x-ray-pump/x-ray-probe spectroscopy

However, the sub-femtosecond XUV pulses currently available do not have sufficient flux for XUV-pump/XUV-probe spectroscopy yet. This is because in this kind of experiments the physical quantity measured as a function of delay between pump and probe pulse relies on a two-photon transition, the probability of which scales with

$$\frac{3}{4} \sigma I_{\text{pump}} \sigma I_{\text{probe}}; \quad (4.1)$$

where $\frac{3}{4}$ is the atomic cross-section of the absorption process and I_{pump} and I_{probe} are the intensities of the driving electro-magnetic wave. Both I_{pump} and I_{probe} are significantly weaker than in the optical regime. Moreover $\frac{3}{4}$ is also reduced by many orders

of magnitude because it scales with ω^6 . Hence, the low two-photon transition probability prevents XUV-pump/XUV-probe experiments from being implemented with currently available sources. A solution of this problem, namely the concept of light-field-controlled XUV photoemission allows to substitute either the XUV pump or the XUV probe pulse by a strong few-cycle laser field, in other words, to employ the XUV pulse as a pump and the light pulse as a probe [69] or vice versa. The basic prerequisite, namely the generation and measurement of isolated sub-femtosecond XUV pulses synchronized to a strong few-cycle light pulse [61], with attosecond precision as it was presented in this work, opens up a route to time-resolved (pump-probe) inner-shell atomic spectroscopy with present day sources. The next section summarizes the relevant concepts.

4.2 Experimental applications

XUV-pump/Visible-probe experiment

In this class of studies the sub-femtosecond XUV pulse serves as a pump pulse to create an inner-shell vacancy. The temporal evolution of the subsequent inner-shell relaxation processes is traced by time-resolved spectroscopy of the emitted Auger electron(s). The modification of the Auger spectrum modified by a few-cycle light field can be measured as a function of t_d (see Fig. 4.2) in the same way as it was done using the photoelectrons. Just as the photoelectrons provided information about the duration of the ionizing XUV pulse, the Auger electrons will provide access to the (few-femtosecond to attosecond) inner-shell relaxation times.

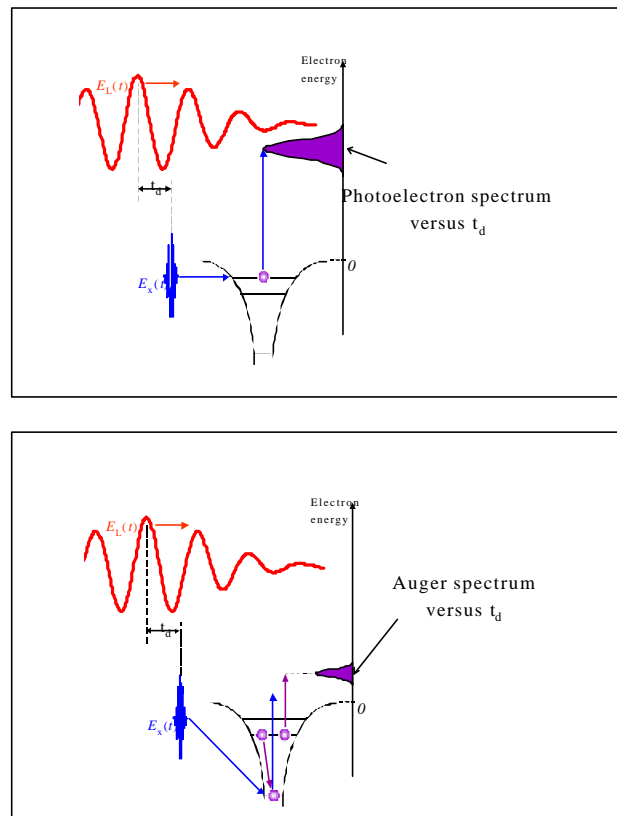


Figure 4.2: XUV-pump/Visible-probe experiment: The duration of emission of photoelectrons lets conclude the duration of the XUV pulse λ_X . The emission time of the Auger electrons provides access to the lifetime of inner-shell vacancies.

Time-resolved ionization dynamics

As an ionization process leads to a shift of electron binding energies, photoelectron spectra can be used to track its temporal evolution. If the probing XUV-pulse is short enough, it is expected that the stepwise evolution of the ionization process according to the electric laser field can be traced.

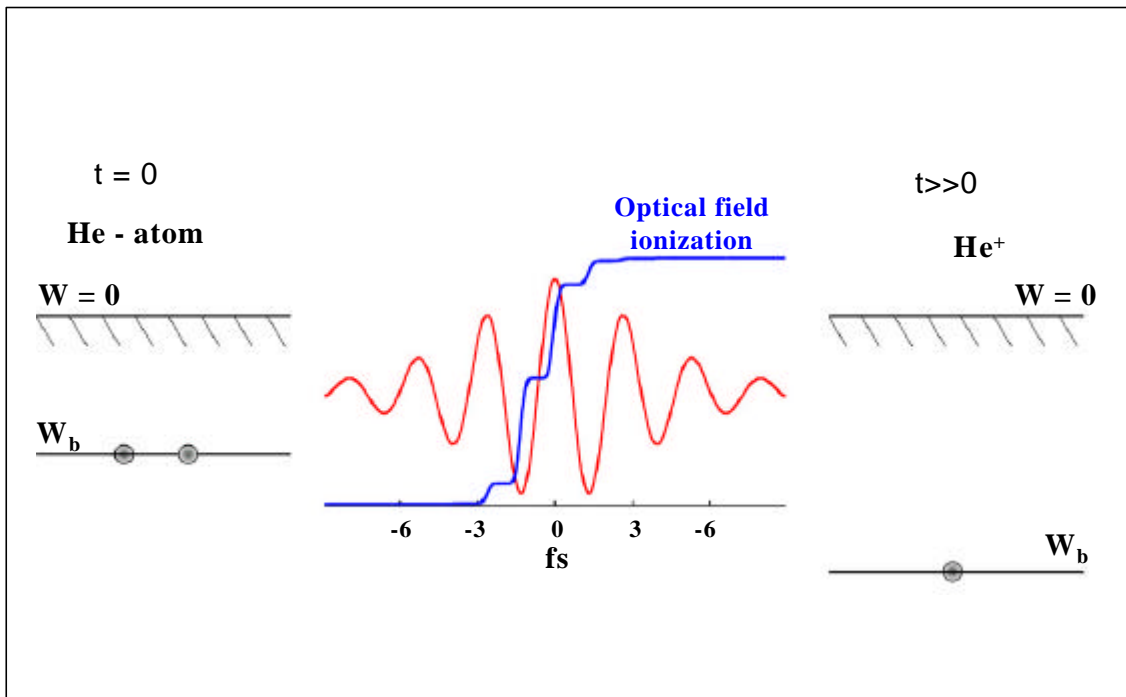


Figure 4.3: Tracing optical field ionization and subsequent electron dynamics in ions.

Figure 4.4 shows preliminary experimental data of the measurement of time-resolved ionization dynamics.

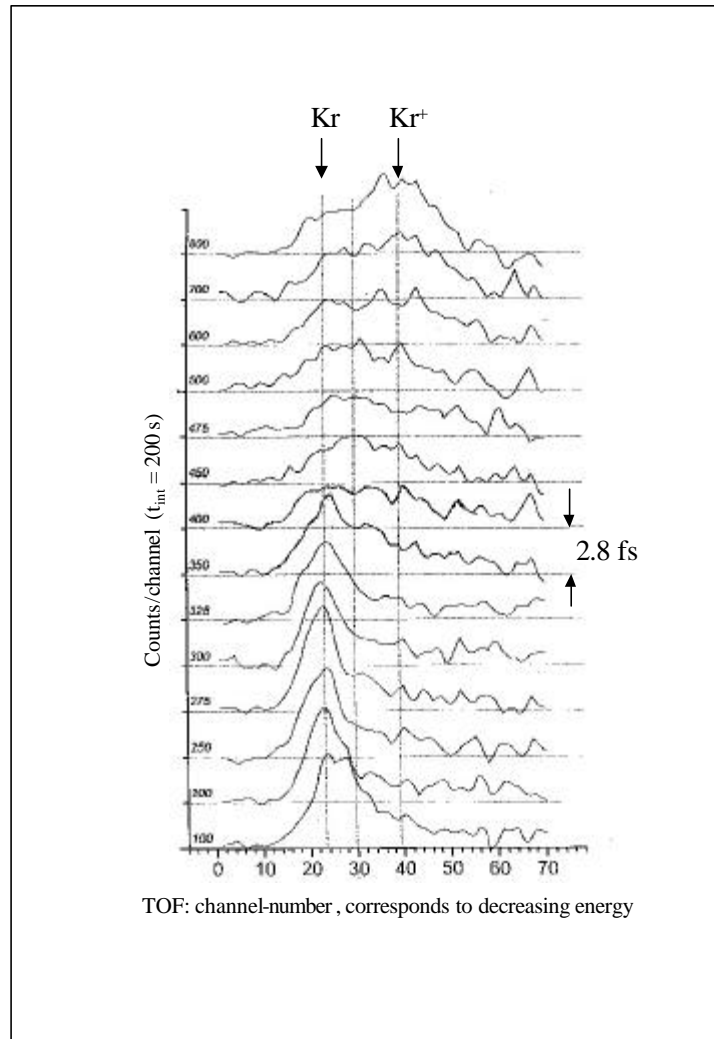


Figure 4.4: Time-resolved measurement of ionization-dynamics using ≈ 2 fs, 90 eV XUV pulses: The curves show XUV photoelectron energy-spectra showing the Kr 4p feature at different instants during ionization by a 7-fs, 780nm laser pulse disappearing and the Kr⁺ 4p peak appearing as the XUV pulse is scanned through the laser pulse. Time is elapsing (in steps of 2.8 fs) upwards on the Figure.

Chapter 5

Conclusions and outlook

The availability of sub-femtosecond XUV pulses set a cornerstone to extend time-resolved spectroscopy into the attosecond domain. For pump/probe experiments, the concept of light-field-controlled XUV photoemission allows to substitute either the XUV pump or the XUV probe pulse by a strong few-cycle laser field without compromising attosecond resolution. This approach vastly relaxes requirements on the XUV pulse fluence, opening the door to attosecond spectroscopy of bound electron dynamics. As few-cycle laser pulses both offer the potential for generating sub-femtosecond XUV bursts and are pretty well synchronized to the latter, the required specifications are fulfilled.

The whole potential of few-cycle laser driven sub-femtosecond pulse generation and light-field-controlled photoemission can only be fully exploited with phase-stabilized few-cycle light. As pointed out in Section 2.2.3 the spectrum and hence the temporal structure of radiation emitted by a few-cycle-driven harmonic source depends sensitively on the absolute phase of the laser pulse φ . The random variation of φ translates into a timing jitter and fluctuations of the energy and duration of the harmonic pulses. Timing jitter between the x-ray pulse and the probe light phase affects the temporal resolution to the same extent as λ_x and T_0 [69]. A control and stabilization to $\varphi = 0$ will have two major advantages: (i) The amount of high-harmonic photons in single XUV bursts will increase and the process of frequency band selection described in Section 2.2.4, which is very sensitive and complex, will be made much easier. (ii) The time of 'birth' of the XUV pulse can be locked to the phase of the fundamental pulse, in other words, one can get rid of any kind of jitter.

An other technical improvement to increase the XUV photon amount has to be made by providing a homogeneous fundamental laser field strength (flat-top profile) over the whole focal spot at the interaction region of HHG. Only under this condition it is possible to gain a unique spectral distribution over the harmonic beam profile (see Section 2.2.2). Such a flat-top beam profile can be formed by a deformable mirror which is able to modulate the incoming gaussian-like beam profile. With the reflective layer seated on a flexible ceramic plate, several piezo-electric actuators can be addressed to modulate the surface. A program reading out the beam profile from an imaging CCD-camera evaluates the data and calculates new values of voltage for the piezo actuators by a genetic algorithm. By running this routine an optimization towards a flat-top fundamental beam profile can be achieved. Basic steps towards controlling such a device have been done and the implementation in the laser system is under construction.

Appendix A

HH intensity measurement device

The program 'HH-Meter' was developed to chart the high harmonic photon flux. The principle of measurement is described in Section 2.2.2. All spectral components of the harmonic radiation drive ionization in the background gas coming from the harmonic target. The ions are collected at a biased wire, leading to a current which is converted into voltage by a self-made I-U converter.

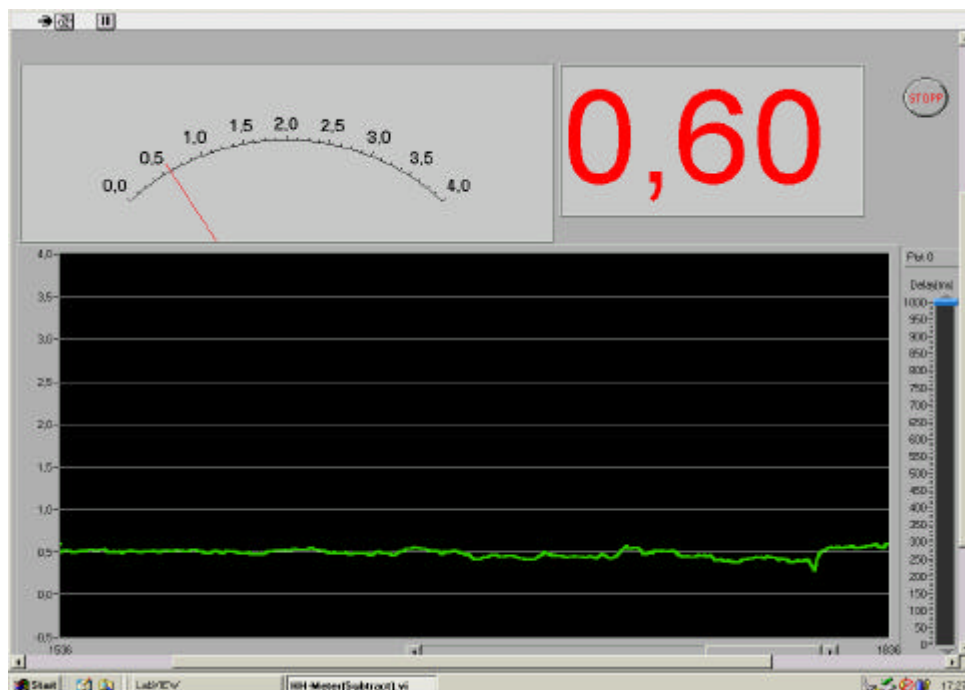


Figure A.1: Front panel of LabVIEW program 'HH-Meter', part of the HH intensity measurement device.

Via a commercial I-O board and the USB interface the program reads out the voltage using standard LabVIEW functional sub-VIs (see Fig. A.2) and charts it as presented in Fig. A.1. As was mentioned in Section 2.2.2, no special wavelength can selectively be measured, however, the whole spectral behaviour lets estimate the one of a certain spectral regime and is a powerful online diagnostics during experiments.

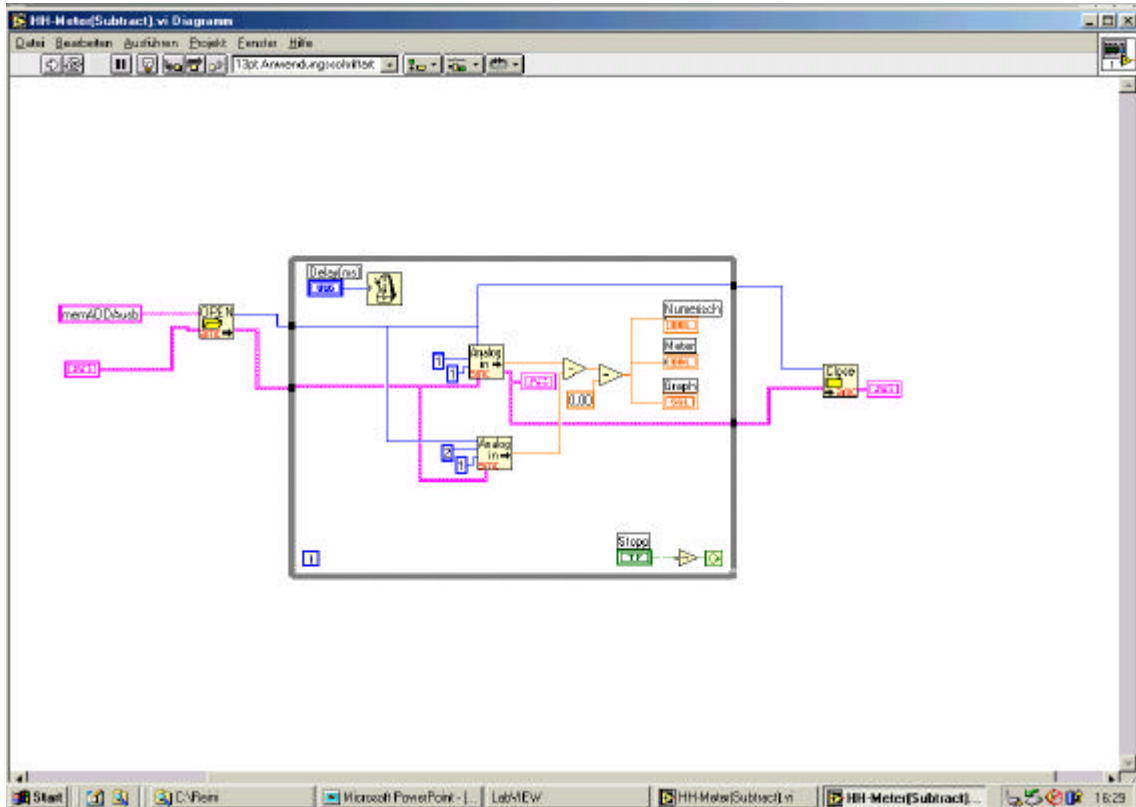


Figure A.2: Functional diagramm of LabVIEW programm 'HH-Meter', part of the HH intensity measurement device.

Appendix B

Control of wide-range piezo stage

The program PIEZO serves as a control of the wide range nanometer precision piezo stage which is used to introduce a temporal delay between the outer and the inner part of the multilayer XUV-mirror mentioned in Section 3.1.2. The electronic driver unit of the piezo stage is supplied by a closed loop control system measuring the position of the piezo stage by a capacity.

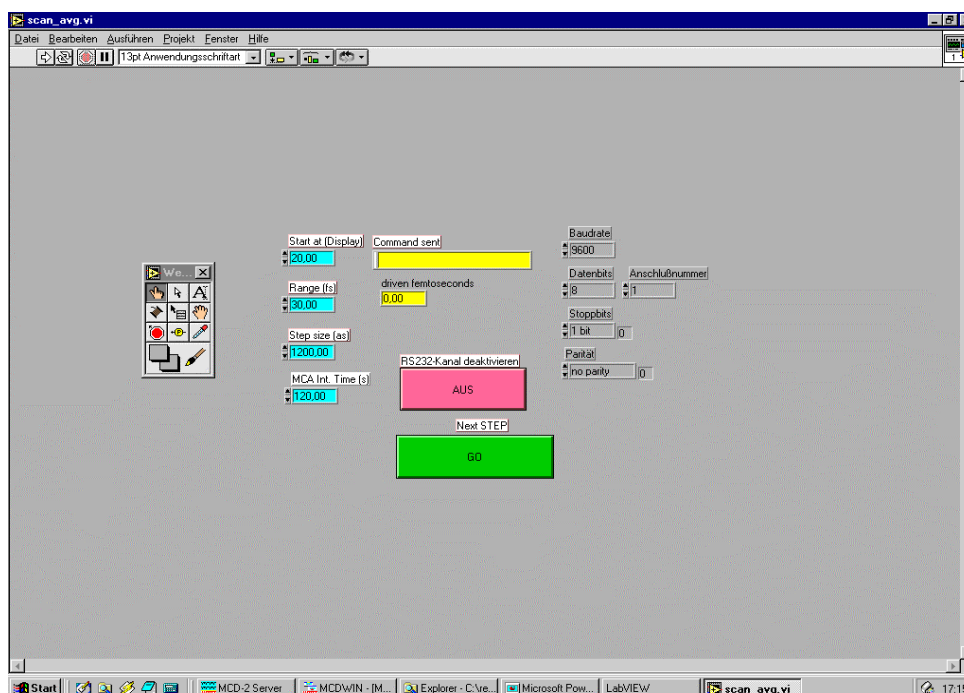


Figure B.1: Front panel of LabVIEW programm 'PIEZO', controlling the wide-range piezo stage

This driver is addressed over the RS232 interface. Using standard LabVIEW functional sub-VIs (see Fig. B.2) the few commands are sent to the driving unit. Optical interferometry monitored over the CMOS camera (see Section 3.1.2) was the base for calibrating the movement commands.

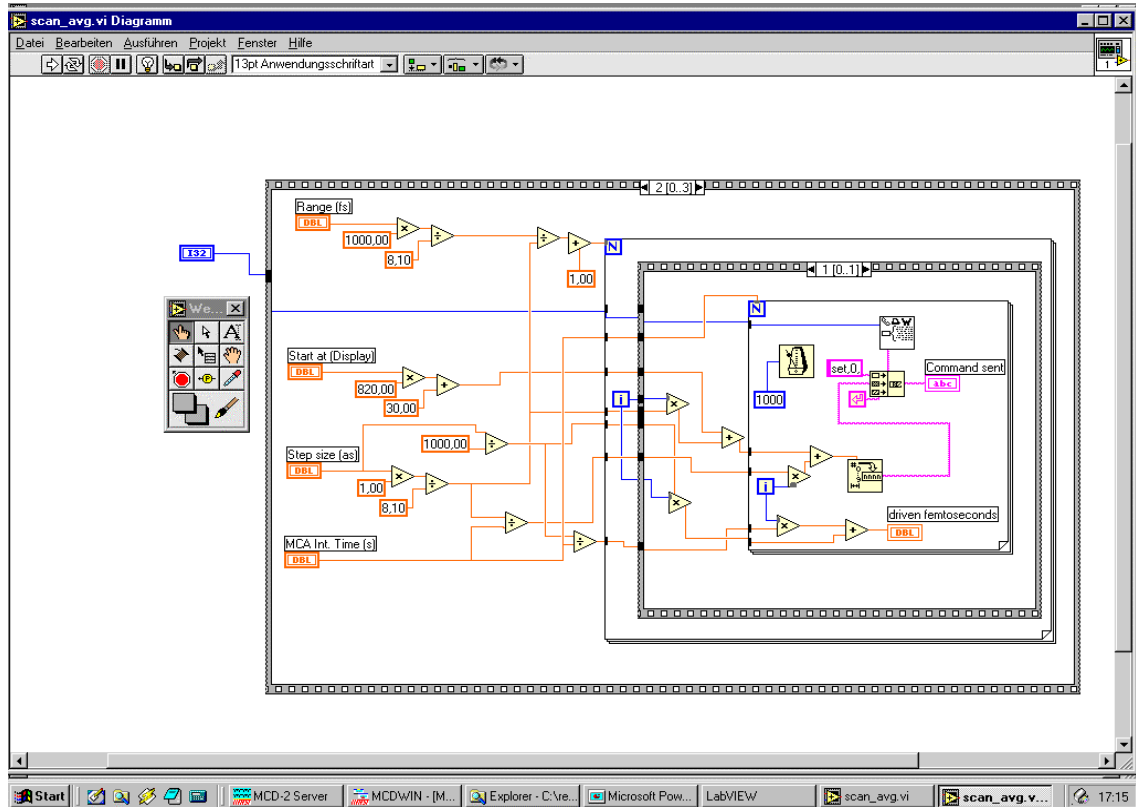


Figure B.2: Functional diagramm of LabVIEW programm 'PIEZO', controlling the wide-range piezo stage

Appendix C

Routine to measure XUV-/VIS cross-correlation online

LabVIEW programm 'CROSS-CORR' both controls the wide range nanometer precision piezo stage (see Appendix B) and reads out the signal coming from the time of flight (TOF) spectrometer via microsphere plate (MSP) detector, time-to-amplitude

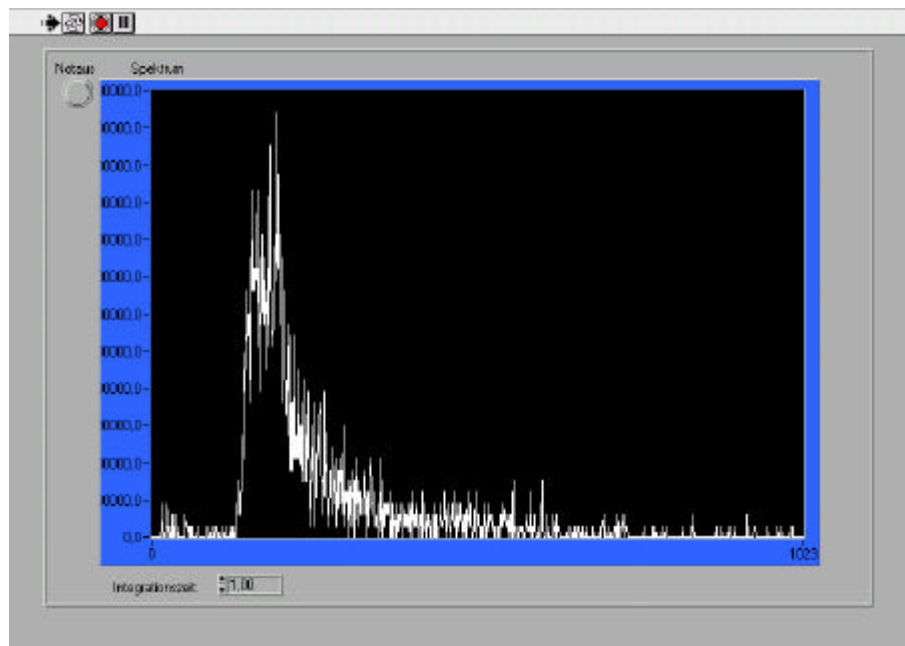


Figure C.1: Front panel of LabVIEW programm 'CROSS-CORR', a routine to measure XUV-/VIS cross-correlation online.

converter (TAC), a multi-channel pulse height analyser, analog/digital converter (ADC) and an I-O card. By selecting the upper and lower limits of the ADC one is able to measure only the high energy spectral tail of the XUV photoelectron spectrum following the spectral broadening as described in Section 3.2.2. Scanning through the time delay between laser and XUV pulses this signal is used as an indicator of time delay, so it is possible to find the temporal overlap of the two beams' intensity maxima without removing the filter plus pellicle. As is shown in Fig. C.2 the program reads out the signal using standard LabVIEW sub-VIs and charts it as shown in Fig. C.1.

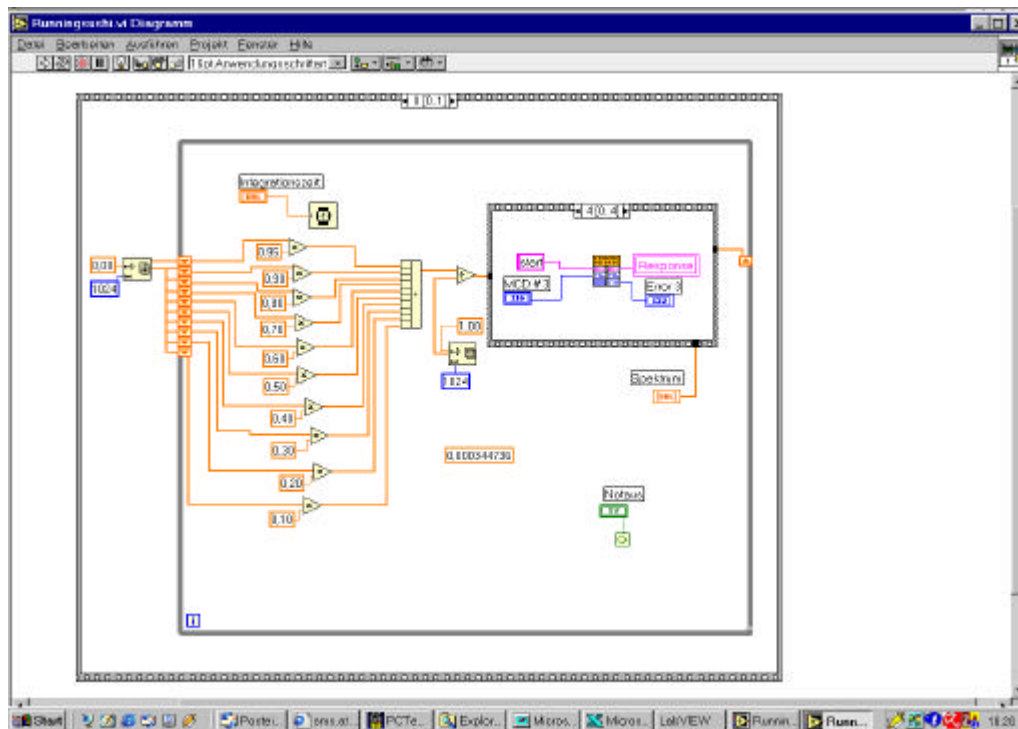


Figure C.2: Functional diagram of LabVIEW programm 'CROSS-CORR', a routine to measure XUV-/VIS cross-correlation online.

Appendix D

Program for measuring cross-correlation scans

LabVIEW programm 'SCAN' addresses the driver of the piezo stage and reads out the signal from the TOF over the I-O card.

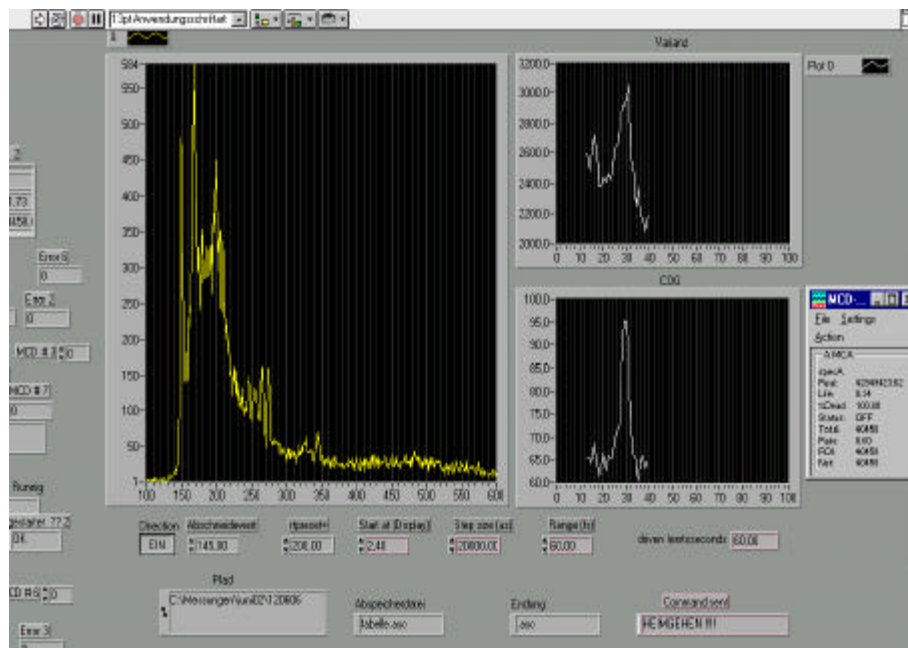


Figure D.1: Front panel of LabVIEW programm 'SCAN', for measuring cross-correlation scans.

It integrates the signal over a time which can be chosen due to the amount of counts per second one gains. After each integration period it drives the piezo stage by a selectable distance (time delay). The measurement data are simultaneously saved into files for further evaluation. During the measurement scan the program calculates the variance and the center of gravity (see Fig. D.1) and charts these two parameters, so that one is able to check whether the measurement scan delivers usable results (or if in contrary e.g. the spatial overlap has been lost). Addressing the piezo stage driver over the RS232 interface and reading out the data from the I-O card is carried out by standard LabVIEW sub-VIs (see Fig. D.2).

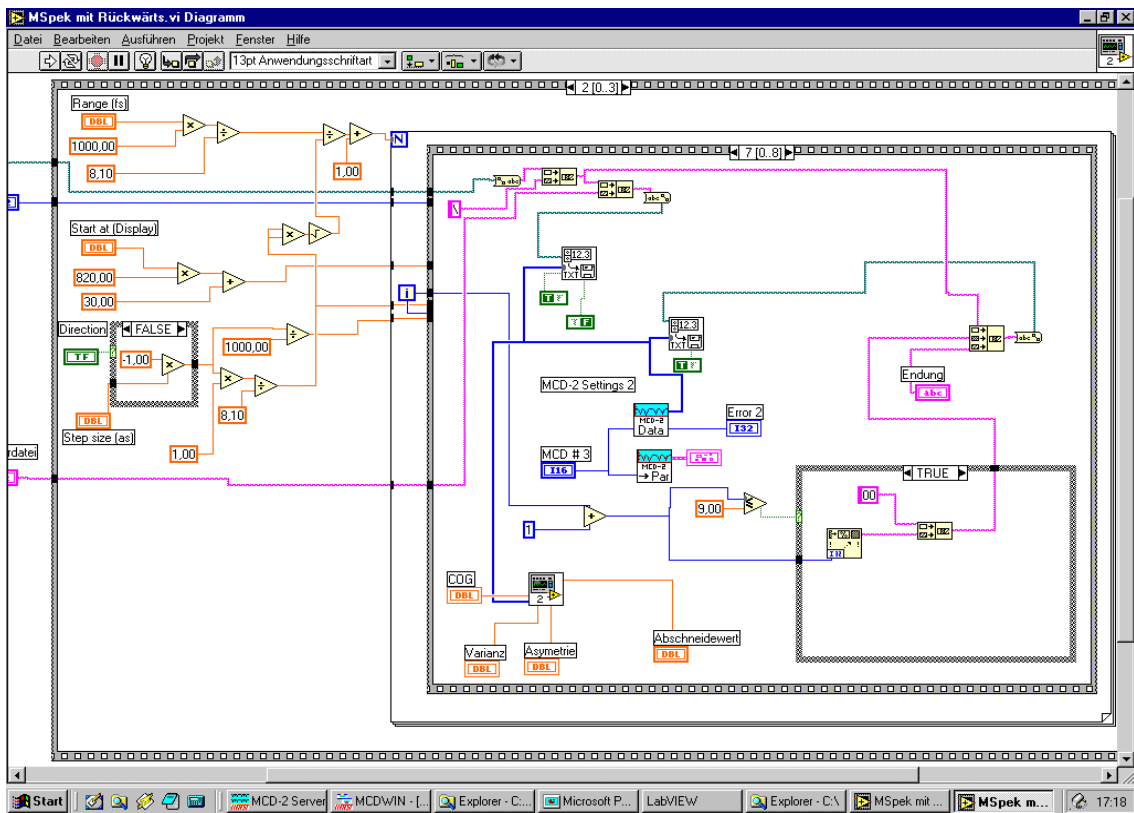


Figure D.2: Functional diagram of LabVIEW programm 'SCAN', for measuring cross-correlation scans.

Bibliography

- [1] A. Zewail, Femtochemistry: atomic-scale dynamics of the chemical bond (adapted from the Nobel Lecture), *J. Phys. Chem. A* **104** 5660-5694 (2000).
- [2] Y. Bhattacharjee, Measuring the immeasurable, *Nature* **412**, 474-476 (2001).
- [3] U. Becker and D.A. Shirley, *VUV and Soft X-Ray Photoionization*, Plenum Press, New York and London, 1996.
- [4] F. Krausz, From femtochemistry to attophysics, *Phys. World* Sept. 41-46 (2001).
- [5] G. Steinmeyer, D.H. Sutter, L. Gallmann, N. Matuschek, U. Keller, *Frontiers in Ultrashort Pulse Generation: Pushing the Limits in Linear and Nonlinear Optics*, *Science* **286**, 1507 (1999).
- [6] T. Brabec and F. Krausz, Intense Few-Cycle Laser Fields: Frontiers of Nonlinear Optics, *Rev. Mod. Phys.* **72**, 545 (2000).
- [7] A. Baltuska, Z. Wei, M.S. Pshenichnikov, D.A. Wiersma, R. Szipäcs, All-Solid-State Cavity-Dumped Sub-5-fs Laser, *Appl. Phys. B* **65**, 175 (1997).
- [8] M. Nisoli, S. Stagira, S. De, O. Svelto, S. Sartania, Z. Cheng, M. Lenzner, Ch. Spielmann, F. Krausz, A Novel High-Energy Pulse Compression System: Generation of Multigigawatt Sub-5-fs Pulses, *Appl. Phys. B* **65**, 189 (1997).
- [9] U. Morgner, F.X. Kärtner, S.H. Cho, Y.Chen, H.A. Haus, J.G. Fujimoto, E.P. Ippen, V. Scheuer, G. Angelow, T. Tschudi, Sub-Two-Cycle Pulses from a Kerr-Lens Mode-Locked Ti:Sapphire Laser, *Opt. Lett.* **24**, 411 (1999).

- [10] A. Shirakawa, I. Sakane, M. Takasaka & T. Kobayashi, Sub-5-fs visible pulse generation by pulse-front-matched noncollinear optical parametric amplification, *Appl. Phys. Letters* **74**, 2268 (1999).
- [11] A. L'Huillier & P. Balcou, High-order harmonic generation in rare gases with a 1-ps 1053-nm laser, *Phys. Rev. Lett.* **70**, 774-777 (1993).
- [12] C. J. Joachain, M. D'Ärr & N. J. Kylstra, Photon emission by He-sup+ in intense ultrashort laser pulses, *Adv. At., Mol., Opt. Phys* **42**, 225 (2000).
- [13] P. Salipires, A. L'Huillier & M. Lewenstein, *Adv. At., Mol., Opt. Phys* **41**, 83 (1999).
- [14] J. J. Macklin, J. D. Kmetec & C. L. Gordon III, High-order harmonic generation using intense femtosecond pulses *Phys. Rev. Lett.* **70**, 766-769 (1993).
- [15] N.A. Papadogiannis, B. Witzel, C. Kalpouzos, D. Charalambidis, Observation of Attosecond Light Localization in Higher Order Harmonic Generation, *Phys. Rev. Lett.* **83**, 4289 (1999).
- [16] P. M. Paul, E. S. Toma, P. Breger, G. Mullot, F. Augé, Ph. Balcou, H. G. Muller & P. Agostini, Observation of a train of attosecond pulses from high harmonic generation *Science* **292**, 1689-1692 (2001).
- [17] M. Ivanov, P. B. Corkum, T. Zuo & A. Bandrauk, Routes to control of intense-field atomic polarizability, *Phys. Rev. Lett.* **74**, 2933-2936 (1995).
- [18] I. P. Christov, M. M. Murnane & H. C. Kapteyn, High-harmonic generation of attosecond pulses in the $\frac{1}{2}$ -cycle regime *Phys. Rev. Lett.* **78**, 1251-1254 (1997).
- [19] Ch. Spielmann, N.H. Burnett, S. Sartania, R. Koppitsch, M. Schnürer, C. Kan, M. Lenzner, P. Wobrauschek, F. Krausz, Generation of Coherent X-Rays in the Water Window Using 5-Femtosecond Laser Pulses, *Science* **278**, 661 (1997).
- [20] M. Drescher, M. Hentschel, R. Kienberger, G. Tempea, Ch. Spielmann, G. Reider, P.B. Corkum, F. Krausz, X-Ray Pulses Approaching the Attosecond Frontier, *Science* **291**, 1923 (2001).

- [21] T. W. Hänsch, A proposed sub-femtosecond pulse synthesizer using separate phase-locked laser oscillators, *Opt. Commun.* **80**, 71 (1990).
- [22] G. Farkas and C. Toth, Proposal for Attosecond Light Pulse Generation Using Laser Induced Multiple-Harmonic Conversion Processes in Rare Gases, *Phys. Lett. A* **168**, 447 (1992).
- [23] S. E. Harris, J.J. Macklin, T.W. Hänsch, Atomic scale temporal structure inherent to high-order harmonic generation, *Opt. Commun.* **100**, 487 (1993).
- [24] S. Sartania, Z. Cheng, M. Lenzner, G. Tempea, Ch. Spielmann, F. Krausz, Generation of 0.1-TW 5-fs Optical Pulses at a 1-kHz Repetition Rate, *Opt. Lett.* **22**, 1562 (1997).
- [25] M. Schnärrer, Z. Cheng, M. Hentschel, G. Tempea, P. Klumpp, T. Brabec, F. Krausz, Absorption-Limited Generation of Coherent Ultrashort Soft-X-Ray Pulses, *Phys. Rev. Lett.* **83**, 722 (1999).
- [26] M. Hentschel, Z. Cheng, F. Krausz & Ch. Spielmann, Generation of 0.1-TW optical pulses with a single-stage Ti:sapphire amplifier at a 1-kHz repetition rate, *Appl. Phys. B* **70**, 161-164 (2000).
- [27] M. Schnärrer, Z. Cheng, M. Hentschel, F. Krausz, T. Wilhein, D. Hambach, G. Schmahl, M. Drescher, Y. Lim, U. Heinzmann, Few-Cycle-Driven XUV Laser Harmonics: Generation and Focusing, *Appl. Phys. B* **70**, S227 (2000).
- [28] Ch. Spielmann, C. Kan, N.H. Burnett, T. Brabec, M. Geissler, A. Scrinzi, M. Schnärrer, F. Krausz, Near-keV coherent X-ray generation with sub-10-fs lasers, *IEEE J. Sel. Top. Quantum Electr.* **4**, 249 (1998).
- [29] M. Lewenstein, Ph. Balcou, M.Y. Ivanov, A. L'Huillier, P.B. Corkum, Theory of High-Harmonic Generation by Low Frequency Laser Fields, *Phys. Rev. A* **49**, 2117 (1994).
- [30] K. J. Schafer and K. C. Kulander, Theory of resonant multiphoton population transfer in xenon, *Phys. Rev. Lett.* **78**, 638 (1997).
- [31] C. Kan, N.H. Burnett, C. Capjack, R. Rankin, Coherent XUV Generation from Gases by Several Cycle Optical Pulses, *Phys. Rev. Lett.* **79**, 2971 (1997).

- [32] A. McPherson, T.S. Luk, M.H.R. Hutchinson, H. Jara, U. Johann, I.A. McIntyre, A.P. Schwarzenbach, K. Boyer, C.K. Rhodes, VUV Fluorescence and Harmonic Generation with Intense Picosecond 248 nm KrF* Radiation, SPIE Proceedings **710**, 103 (1987).
- [33] X. Li, A. L'Huillier, M. Ferray, L.A. Lompre & G. Mainfray, Multiple-harmonic generation in rare gases at high laser intensity, Phys. Rev. A **39**, 5751 (1989).
- [34] N. Sarukura, K. Hata, T. Adachi, R. Nodomi, M. Watanabe, & S. Watanabe, Coherent soft X-ray generation by the harmonics of an ultrahigh-power KrF laser, Phys. Rev. A **43**, 1669 (1991).
- [35] J. K. Crane, M.D. Perry, S. Hermann & R. W. Falcone, High-field harmonic generation in helium, Opt. Lett. **917**, 1256 (1992).
- [36] M. E. Faldon, M. H. R. Hutchinson, J.P. Marangos, J.E. Muett, R. A. Smith, J. W. G. Tisch and C. G. Wahlström, Studies of time-resolved harmonic generation in intense laser fields in xenon, J. Opt. Soc. Am. B **9**, 2094 (1992).
- [37] K. Kondo, N. Sarukura, K. Sajiki & S. Watanabe, Terawatt class Ti:sapphire laser, Phys. Rev. A **47**, R2480 (1993).
- [38] M. D. Perry & J. K. Crane, High-order harmonic emission from mixed fields, Phys. Rev. A **48**, R4051 (1993).
- [39] C. G. Wahlström, J. Larsson, A. Persson, T. Starczewski, S. Svanberg, P. Salieres, Ph. Balcou & A. L'Huillier, High-order harmonic generation in rare gases with an intense short-pulse laser, Phys. Rev. A **48**, 4709 (1993).
- [40] J. W. Tisch, R. A. Smith, J. E. Muett, M. Ciarocca, J. P. Marangos & M. H. Hutchinson, Angularly-resolved high-order harmonic generation in helium, Phys. Rev. A **49**, R28 (1994).
- [41] K. Myazaki & H. Takada, High-order harmonic generation in the tunneling regime, Phys. Rev. A **52**, 3007 (1995).
- [42] T.D. Donnelly, T. Ditmire, K. Neumann, M.D. Perry, R.W. Falcone, High-Order Harmonic Generation in Atom Clusters, Phys. Rev. Lett. **76**, 2472 (1996).

- [43] S. X. Hu and Z.Z. Xu, Enhanced harmonic emission from ionized clusters in intense laser pulses, *Appl. Phys. Lett.* **71**, 2605 (1997).
- [44] M.Y. Ivanov and P.B. Corkum, Generation of High-Order Harmonics from Inertially Confined Molecular Ions, *Phys. Rev. A* **48**, 580 (1993).
- [45] Y. Liang, S. August, S. L. Chin, Y. Beaudoin & M. Chaker, High harmonic generation in atomic and diatomic molecular gases using intense picosecond laser pulses—a comparison, *Phys. Rev. B* **27**, 5119 (1994).
- [46] P. B. Corkum, Plasma perspective on strong-field multiphoton ionization, *Phys. Rev. Lett* **71**, 1994 (1993).
- [47] L.V. Keldysh, Ionization in the Field of a Strong Electromagnetic Wave, *Sov. Phys. JETP* **20**, 1307 (1965).
- [48] K.C. Kulander, K.J. Schafer, J.L. Krause, Theoretical Model for Intense Field High-Order Harmonic Generation in Rare Gases, *Laser Phys.* **3**, 359 (1993).
- [49] K.C. Kulander and B.W. Shore, Calculations of Multiple-Harmonic Conversion of 1064-nm Radiation in Xe, *Phys. Rev. Lett.* **63**, 524 (1989).
- [50] A. L'Huillier, K.J. Schafer, K.C. Kulander, High-Order Harmonic Generation in Xenon at 1064 nm: The Role of Phase Matching, *Phys. Rev. Lett* **66**, 2200 (1991).
- [51] G. Tempea, M. Geissler, M. Schnürer, T. Brabec, Self-Phase-Matched High Harmonic Generation, *Phys. Rev. Lett.* **84**, 4329 (1999).
- [52] E. Constant, D. Garzella, P. Breger, E. M'euvel, Ch. Dorrer, C. Le Blanc, F. Salin, P. Agostini, Optimizing High Harmonic Generation in Absorbing Gases: Model and Experiment, *Phys. Rev. Lett.* **82**, 1668 (1999).
- [53] Y. Kobayashi, T. Sekikawa, Y. Nabekawa, S. Watanabe, 27-fs Extreme Ultraviolet Pulse Generation by High-Order Harmonics, *Opt. Lett.* **23**, 64 (1998).
- [54] E.S. Toma, H.G. Muller, P.M. Paul, P. Breger, M. Cheret, P. Agostini, C. Le Blanc, G. Mullot, G. Cheriaux, Ponderomotive Streaking of the Ionization Po-

- tential as a Method for Measuring Pulse Durations in the XUV Domain with fs Resolution, *Phys. Rev. A* **62**, 061801(R) (2000).
- [55] A. de Bohan, P. Antoine, D.B. Milosevic & B. Piroux, Phase-dependent harmonic emission with ultrashort laser pulses, *Phys. Rev. Letters* **81**, 1837 (1998).
- [56] P. Antoine, A. LHuillier & M. Lewenstein, Attosecond Pulse Trains Using High-Order Harmonics, *Phys. Rev. Lett.* **77**, 1234 (1996).
- [57] N. Milosevic, A. Scrinzi, & T. Brabec, Ab initio numerical calculation of attosecond pulse generation, *Phys. Rev. Lett.* **88**, 093905 (1996).
- [58] P.B. Corkum, V.D. Taranukhin, E. Constant, Measuring Subfemtosecond Pulses, *CLEO'94, Proceedings* **8**, 293 (1994).
- [59] P.B. Corkum, N.H. Burnett, M.Y. Ivanov, Sub-Femtosecond Pulses, *Opt. Lett.* **19**, 1870 (1994).
- [60] E. Constant, V.D. Taranukhin, A. Stolow, P.B. Corkum, Methods for the measurement of the duration of high-harmonic pulses, *Phys. Rev. A* **56**, no.5, 3870 (1997).
- [61] M. Hentschel, R. Kienberger, Ch. Spielmann, G. A. Reider, N. Milosevic, T. Brabec, P. B. Corkum, U. Heinzmann, M. Drescher & F. Krausz, Attosecond metrology, *Nature* **414**, 509-513 (2001).
- [62] J.M. Schins, P. Breger, P. Agostini, R.C. Constantinescu, H.G. Muller, G. Grillon, A. Antonetti, A. Mysyrowicz, Observation of Laser-Assisted Auger Decay in Argon, *Phys. Rev. Lett.* **73**, 2180 (1994).
- [63] J.M. Schins, P. Breger, P. Agostini, R.C. Constantinescu, H.G. Muller, A. Bouhal, G. Grillon, A. Antonetti, A. Mysyrowicz, Cross-Correlation Measurements of Femtosecond Extreme-Ultraviolet High-Order Harmonics, *J. Opt. Soc. Am. B* **13**, 197 (1996).
- [64] T.E. Glover, R.W. Schoenlein, A.H. Chin, C.V. Shank, Observation of Laser Assisted Photoelectric Effect and Femtosecond High Order Harmonic Radiation, *Phys. Rev. Lett.* **76**, 2468 (1996).

- [65] A. Bouhal, R. Evans, G. Grillon, A. Mysyrowicz, P. Breger, P. Agostini, R.C. Constantinescu, H.G. Muller, D. von-der-Linde, Cross-Correlation Measurement of Femtosecond Noncollinear High-Order Harmonics, *J. Opt. Soc. Am. B* **14**, 950 (1997).
- [66] M. Kitzler, N. Milosevic, A. Scrinzi & T. Brabec Theory of Attosecond streak camera, *Phys. Rev. Lett.* **88**, 173904 (2002).
- [67] J. Itatani, F. Quéré, G. L. Yudin, M. Yu. Ivanov, F. Krausz. & P. B. Corkum, Attosecond streak camera, *Phys. Rev. Lett.* **88**, 173903 (2002).
- [68] A. Poppe, R. Holzwarth, A. Apolonski, G. Tempea, Ch. Spielmann, T. W. Hänsch & F. Krausz, Few-cycle optical waveform synthesis, *Appl. Phys. B* **72**, 373-376 (2001). Published online December 13, 2000; 10.1007/s003400000526.
- [69] F. Krausz, Attosecond spectroscopy comes of age, *Optics & Photonic News*, in press

Curriculum vitae

The author was born on May 25th 1971 in Graz, Austria. After having finished his High School education in 1989, he passed his military service being trained as an officer of mountain infantry.

After that he passed his studies of Electrical Engineering at Vienna University of Technology, where he graduated in 1999 as Diplom-Ingenieur (equivalent to master) in Electrical Engineering. The title of the thesis is: 'Erstellung eines automatisierten Meßsystems zur Röntgenspektralanalyse', 'Construction of an automatized measurement-system for spectroscopy in the x-ray regime'.

Since 1999 the author is working on the Dissertation towards Doctor of Technology (equivalent to PhD) at the Institut für Photonik at Vienna University of Technology.

Research interests are: Laser physics and technology; Laserdriven X-ray sources; Ultrafast Laser-techniques; Strong field laser plasma interactions.

Publications and contributions to conferences can be found in chapter Summary.

Lebenslauf

Der Autor wurde am 25. Mai 1971 in Graz geboren. Nach Volks- und Mittelschulbesuch in Salzburg und Saalfelden maturierte er 1989 an der Höheren Internatsschule des Bundes in Saalfelden mit Auszeichnung. Anschließend diente er im Österreichischen Bundesheer als Einjährig Freiwilliger und wurde zum Milizoffizier, derzeitiger Dienstgrad Oberleutnant, ausgebildet.

Das Studium der Elektrotechnik an der Technischen Universität Wien wurde 1999 mit dem Akad. Grad Diplomingenieur abgeschlossen. Das Thema der Diplomarbeit am Institut für Photonik, TU Wien, unter Leitung von Univ.-Prof. Dr. Ferenc Krausz war 'Erstellung eines automatisierten Messsystems zur Röntgenspektroanalyse'

Seit 1999 arbeitet der Autor an seiner Dissertation 'Sub-Femtosecond XUV-Pulse Generation and Measurement' unter Leitung von Univ.-Prof. Dr. Ferenc Krausz am Institut für Photonik, TU Wien.

Seit Mai 2002 ist der Autor ebendort als Wissenschaftlicher Mitarbeiter in Ausbildung beschäftigt.

Das wissenschaftliche Interesse des Autors konzentriert sich auf: Laser-Physik und -Technik, Ultrakurzpuls-Lasertechnik, Laser-getriebene Röntgenquellen und Laser-Plasma Interaktionen.

Publikationen und Konferenzbeiträge finden sich im Kapitel 'Summary'.